Astron. Astrophys. 342, 69–86 (1999)

ASTRONOMY AND ASTROPHYSICS

# The temporal characteristics of the TeV gamma-radiation from Mkn 501 in 1997

## I. Data from the stereoscopic imaging atmospheric Cherenkov telescope system of HEGRA

**F.A. Aharonian[1], A.G. Akhperjanian[7], J.A. Barrio[2,3], K. Bernlöhr[1,⋆], H. Bojahr[6], J.L. Contreras[3], J. Cortina[3], A. Daum[1], T. Deckers[5], V. Fonseca[3], J.C. Gonzalez[3], G. Heinzelmann[4], M. Hemberger[1], G. Hermann[1,⋆⋆], M. Heß[1], A. Heusler[1], W. Hofmann[1], H. Hohl[6], D. Horns[4], A. Ibarra[3], R. Kankanyan[1,7], O. Kirstein[5], C. Köhler[1], A. Konopelko[1,⋆⋆⋆], H. Kornmeyer[2], D. Kranich[2], H. Krawczynski[1,4], H. Lampeitl[1], A. Lindner[4], E. Lorenz[2], N. Magnussen[6], H. Meyer[6], R. Mirzoyan[2], A. Moralejo[3], L. Padilla[3], M. Panter[1], D. Petry[2,6,†], R. Plaga[2], A. Plyasheshnikov[1,†], J. Prahl[4], G. Pühlhofer[1], G. Rauterberg[5], C. Renault[1], W. Rhode[6], V. Sahakian[7], M. Samorski[5], D. Schmele[4], F. Schröder[6], W. Stamm[5], H.J. Völk[1], B. Wiebel-Sooth[6], C. Wiedner[1], M. Willmer[5], and H. Wirth[1]**

[1] Max-Planck-Institut für Kernphysik, Postfach 103980, D-69029 Heidelberg, Germany
[2] Max-Planck-Institut für Physik, Föhringer Ring 6, D-80805 München, Germany
[3] Universidad Complutense, Facultad de Ciencias Físicas, Ciudad Universitaria, E-28040 Madrid, Spain
[4] Universität Hamburg, II. Institut fuer Experimentalphysik, Luruper Chausse 149, D-22761 Hamburg, Germany
[5] Universität Kiel, Institut für Kernphysik, Olshausenstrasse 40, D-24118 Kiel, Germany
[6] Universität Wuppertal, Fachbereich Physik, Gaußstrasse 20, D-42097 Wuppertal, Germany
[7] Yerevan Physics Institute, Alikhanian Br. 2, 375036 Yerevan, Armenia

Received 12 August 1998 / Accepted 21 October 1998

**Abstract.** During 1997, the BL Lac Object Mkn 501 was the brightest known object in the TeV $\gamma$-ray sky. The emission was characterized by dramatic variations in intensity with a mean flux exceeding by a factor of three the steady $\gamma$-ray flux of the Crab Nebula. The stereoscopic HEGRA system of 4 Imaging Atmospheric Cherenkov Telescopes, with an energy threshold of about 500 GeV, an angular resolution of 0.1°, an energy resolution of $20\%$, and a flux sensitivity $\nu F_\nu$ at 1 TeV of $10^{-11}\,\mathrm{ergs/cm^2sec} \simeq$ 1/4 Crab for 1 hour of observation time ($\mathrm{S}/\sqrt{\mathrm{B}}{=}5\sigma$), has been used in 1997 for a comprehensive study of the spectral and temporal characteristics of the TeV $\gamma$-ray emission from Mkn 501 on time scales of several hours or less. In this paper (Part I) the $\gamma$-ray fluxes and spectra on a diurnal basis during the period March to October 1997 are presented. Furthermore, the correlation of the TeV emission with the flux measured by the RXTE All Sky Monitor in the energy range from 2 to 12 keV are studied. Finally the implications of these results on the physics of relativistic jets in BL Lac objects are briefly discussed. The companion paper (Part II) describes the results from the stand alone telescopes CT1 and CT2.

**Key words:** gamma rays: observations – galaxies: BL Lacertae objects: individual: Mkn 501

### 1. Introduction

Mrk 501 was discovered as a source of TeV-$\gamma$-radiation in 1995 by the Whipple group (Quinn et al. 1996). The observation was confirmed later by the HEGRA collaboration (Bradbury et al. 1997). Together with two other extragalactic TeV $\gamma$-ray sources detected so far, Mrk 421 (Punch et al. 1992; Petry et al. 1996) and 1ES 2344+514 (Catanese et al. 1998), Mrk 501 belongs to a sub-population of Active Galactic Nuclei (AGNs), the so-called BL Lac objects. Flux variability on various time scales, ranging from dramatic flares of Mrk 421 in May 1996 with durations of about 1 h (Gaidos et al. 1996) to a state of high flaring activity of Mrk 501 which lasted several months (e.g. Protheroe et al. 1997), is a characteristic feature of the TeV emission observed from BL Lac objects. This agrees well with the general properties of BL Lac objects – highly variable AGNs without significant optical line emission, but showing a strong nonthermal (synchrotron) component of radiation from radio to X-ray wavelengths (e.g. Urry & Padovani 1995).

The correlated flares of BL Lac objects in the keV energy band and in the TeV energy band, discovered for the first time

*Send offprint requests to*: H. Krawczynski (Henric.Krawczynski@mpi-hd.mpg.de)

⋆ Now at Forschungszentrum Karlsruhe, P.O. Box 3640, D-76021 Karlsruhe, Germany

⋆⋆ Now at Enrico Fermi Institute, University of Chicago, 933 East 56th Street, Chicago, IL 60637, USA

⋆⋆⋆ *Permanent address:* Altai State University, Dimitrov Street 66, 656099 Barnaul, Russia

† Now at Universidad Autónoma de Barcelona, Institut de Física d'Altes Energies, E-08193 Bellaterra, Spain

during simultaneous observations of Mrk 421 by the Whipple and ASCA detectors (Takahashi et al. 1996; Buckley et al. 1996), strongly support the commonly accepted view that both components originate in a relativistic jet, with Doppler factors $\delta_{\rm j} \geq 5$, due to synchrotron and inverse Compton (IC) radiation of the same population of ultrarelativistic electrons (for a review see e.g. Ulrich et al. 1997). Since in the Thomson regime the IC cooling time $t_{\rm IC} = -E_{\rm e}/({\rm d}E_{\rm e}/{\rm d}t)$ is proportional to $1/E_{\rm e}$, and since the Compton scattering boosts ambient photons with energies $\epsilon_0$ up to $E_\gamma \propto \epsilon_0 \cdot E_{\rm e}^2$, the characteristic time of $\gamma$-ray emission decreases with energy as $\propto E_\gamma^{-1/2}$. This explains in a natural way the less dramatic variations of the MeV/GeV $\gamma$-ray fluxes during the keV/TeV flares; the relatively low energy electrons, responsible for the GeV IC photons as well as for the optical/UV synchrotron radiation do not respond as rapidly to changes of the physical conditions in the jets as the high energy electrons do. In addition, the expected hard spectra of IC radiation below 100 GeV explain the low fluxes of GeV $\gamma$-rays from Mrk 421, and their non-detection by EGRET in the case of Mkn 501 and 1ES 2344+514. This implies that the VHE $\gamma$-ray region, combined with X-ray observations, is likely to be the most important window of the electromagnetic spectrum to infer the highly non-stationary processes of particle acceleration and their radiation in BL Lac objects. Imaging Atmospheric Cherenkov Telescope (IACT) detectors, characterized by large effective detection areas of $\sim 10^5\,{\rm m}^2$ and an effective suppression of the background of cosmic rays, are well suited to access this very informative "TeV" channel. This was convincingly demonstrated by the Mkn 501 observations with several Cherenkov telescopes located in the Northern Hemisphere during the extreme activity of the source in 1997 (Protheroe et al. 1997).

During the first two years after its discovery as a TeV $\gamma$-ray source, Mkn 501 showed rather low fluxes at a level significantly below the Crab flux (Quinn et al. 1996; Bradbury et al. 1997). However, in March 1997 the source went into a state of highly variable and strong emission with maximum fluxes roughly 10 times that of the Crab. According to the All Sky Monitor (ASM) on board the *Rossi X-Ray Timing Explorer* (RXTE) (Remillard & Levine 1997), the high X-ray activity of the source started in March 1997 and continued until October 1997. Apparently the period of high activity coincided with the period of the visibility of the source by ground-based optical instruments. Thus it was possible to continuously monitor the source during this extremely bright emission period with several IACTs, i.e. with CAT (Barrau et al. 1997), HEGRA (Aharonian et al. 1997a), TACTIC (Bhat et al. 1997), Whipple (Catanese et al. 1997), and the Telescope Array (Hayashida et al. 1998).

The HEGRA experiment is located on the Roque de los Muchachos on the Canary Island of La Palma, (lat. 28.8° N, long. 17.9° W, 2200 m a.s.l.). The HEGRA collaboration operates 6 Cherenkov telescopes. A system of at present four telescopes (telescopes CT3, CT4, CT5, and CT6) is used as a single detector for stereoscopic air shower observations (Daum et al. 1997). The two telescopes, CT1 (Mirzoyan et al. 1994; Rauterberg et al. 1995) and CT2 (Konopelko et al. 1996), are currently operated each as independent detectors. The IACT system is characterized by a high sensitivity and excellent spectroscopic capabilities. The stand alone telescopes CT1 and CT2 have been used to considerably extend the Mkn 501 time coverage, in particular during moonshine periods, when the stereoscopic system was not operated.

In this paper (Part I) the results obtained from the IACT system data are presented. The companion paper (Part II) describes in detail the results from CT1 and CT2 data.

The basic concept of the IACT array is the *stereoscopic approach* based on simultaneous detection of air showers by $\geq$ 2 telescopes under widely differing viewing angles. With the stereoscopic technique an angular resolution of $0.1^\circ$ per photon, an energy resolution of $20\%$ per photon, and a suppression of the isotropic cosmic ray background on the trigger level and by image analysis by a factor of the order of 100 is achieved. Thus $\gamma$-ray observations with unprecedented signal to noise ratio and excellent spectroscopic capabilities are possible. Furthermore, since a hardware trigger requiring the coincident detection of air showers by at least two telescopes strongly suppresses triggers caused by the night sky background light or by local muons, the energy threshold of a stereoscopic telescopes system is mainly limited by Cherenkov photon statistics. As a consequence, the IACT system achieves an energy threshold as low as 500 GeV despite the relatively small size of the telescope mirrors of $8.5\,{\rm m}^2$ (the energy threshold is defined as the energy at which the $\gamma$-ray detection rate peaks for Crab type spectra with differential photon indices of $\sim -2.5$). The flux sensitivity of the IACT system for episodic TeV $\gamma$-ray phenomena with durations of the order of 1 h is about 1/4 Crab[1] (for S/$\sqrt{\rm B}$=5$\sigma$), which corresponds to a $\nu\,F_\nu$-flux at 1 TeV of $\sim 10^{-11}\,{\rm erg/cm^2 s}$. This energy flux sensitivity combines nicely with the comparable energy flux sensitivities of the current X-ray instruments like ASCA, BeppoSAX and RXTE for the study of the high energy emission of BL Lacs, especially of Mkn 501 and of Mkn 421. These two sources proved to release a comparable amount of nonthermal energy in X-rays and in TeV $\gamma$-rays, with an average energy flux in both channels exceeding $\sim 10^{-11}\,{\rm erg/cm^2 s}$. During strong flares of these sources with fluxes up to 10 Crab, a 2 minute exposure is sufficient for the IACT system to detect a statistically significant $\gamma$-ray signal, and a 1 h exposure suffices for a measurement of the differential energy spectrum.

This paper is organized as follows: Hardware issues are briefly summarized in Sect. 2. Analysis methods are presented in Sect. 3. Subsequently, the results concerning the TeV-$\gamma$-ray emission from Mkn 501 in 1997 are discussed. In Sect. 4 the 1997 light curve of Mkn 501 is presented and possible correlations between the flux amplitude and the spectral slope are explored. The most rapid time scales of flux variability are discussed in Sect. 5. The correlation of the TeV-fluxes with the keV-fluxes as measured with the RXTE All Sky Monitor are

[1] In the case of the Crab Nebula, the IACT system currently gives, after cuts, $\simeq$50 $\gamma$-rays per hour over a flat background of 6 events per hour.

studied in Sect. 6. Implications on models of the non-thermal $\gamma-$radiation from BL Lac objects are discussed in Sect. 7.

## 2. The IACT system of HEGRA

The HEGRA telescope system consists presently of 4, in the near future of 5, identical IACTs – one at the center and 3 (in future 4) at the corners of a 100 m by 100 m square area. The multi-mirror reflector of each telescope has an area of 8.5 $m^2$. Thirty front aluminized and quartz coated spherical mirrors of 60 cm diameter and of 4.9 m focal length are independently mounted on an almost spherical frame of an alt-azimuth mount, following the design of Davies and Cotton. Each telescope is equipped with a 271 channel camera of 0.25° pixel size resulting in an effective field of view of 4.3°. The PMT pulses are fed into trigger electronics and into shapers followed by 120 MHz flash analog-to-digital converters (FADCs). A multilevel trigger demands *at least two adjacent pixels* in each of *at least 2 telescopes* (Bulian et al. 1998). The topological "next-neighbor" condition of two *adjacent* pixels reduces the number of night sky background triggers. In the following analysis we use the software trigger condition of at least two telescopes with images with more than 40 photoelectrons.

At the beginning of each night, the camera is flat-fielded using an UV laser at each telescope to illuminate a scintillator via an optical cable. The scintillator emits a spectrum with peak emission in the near-UV and blue, similar to atmospheric Cherenkov light. An absolute calibration of the system has been performed with a direct laser measurement and a calibrated low-power photon detector (Fraß et al. 1997). This measurement has determined the conversion factor from photons to FADC counts with an accuracy of 10%.

The pointing of the telescopes is checked on a regular basis with so called "point runs" (Pühlhofer et al. 1997), where a section of the sky surrounding a bright star is scanned. The pointing of each telescope is inferred from the currents measured in the PMTs surrounding the image of the star. After applying the resulting pointing correction function, an effective pointing accuracy of better than 0.01° is achieved. This accuracy has been experimentally confirmed with $\gamma$-ray data from the Crab Nebula and Mkn 501 (Pühlhofer et al. 1997).

The first system telescope, called CT3, was installed in December 1995. Subsequently CT4 started operation in July 1996, CT5 in September 1996, and CT6 in November 1996. The array of 4 telescopes is operational since end of November 1996. Since then, minor changes of the hardware were carried out. These are summarized in Table 1. In the following, HEGRA data from March 1997 to October 1997 are used. The relevant hardware changes are (i) a mirror adjustment of CT3 and CT4 on May 12th, 1997 and (ii) the incorporation of the topological next-neighbour trigger condition on hardware level for CT3 and CT6 as well, and a reduction of the single pixel trigger threshold for all IACTs from 10 to 8 photoelectrons on June 24th, 1997. CT4 and CT5 had been operated with the next-neighbour trigger condition from the very beginning. These changes divide the Mkn 501 1997 data into 3 groups (period I - period III). In the next subsection it will be shown how the data is corrected for these changes by the use of detailed Monte Carlo simulations.

**Table 1.** The IACT system of HEGRA - Hardware changes during 1996 and 1997.

| Date | Hardware Changes Performed | Data-period |
|---|---|---|
| 27.11.1996 | Start of 4-telescope system CT3, CT6: 2 pixel trigger, CT4, CT5: 2 pixel topological trigger, single pixel threshold 10 p.e. for all CTs | I |
| 12.05.1997 | adjustment of telescope mirrors | II |
| 24.06.1997 | 2 pixel topological trigger and single pixel threshold 8 p.e. for all CTs | III |
| 16.10.1997–15.11.1998 | CT4 not operational due to fire | IV |

**Table 2.** Efficiencies averaged over the wavelength region from 300 to 600 nm.

| Reason | Efficiency |
|---|---|
| Atmospheric transmission | 0.84 |
| Mirror Reflectivity | 0.88 |
| Plexiglas and Funnel transmission | 0.81 |
| Quantum efficiency | 0.18 |
| Total, Cherenkov Photons to FADC channels | 0.10 |

## 3. Analysis of the IACT system data

### *3.1. Monte Carlo simulations*

The Monte Carlo simulation (Konopelko et al. 1998) is divided into two steps. First, the air showers are simulated and the Cherenkov photons hitting one telescope are stored on mass storage devices. Thereafter the detector simulation is carried out. This method has the advantage that it is possible to use the same simulated showers with different detector setups. The air shower simulation is based on the ALTAI code. The results of the code have been tested against results of the CORSIKA code which gave for hadron induced air showers excellent agreement in all relevant observables, e.g., in the predicted detection rates and in the distribution of the image parameters (Hemberger 1998). The detector simulation (Hemberger 1998) accounts for the absorption of Cherenkov photons in the atmosphere due to ozone absorption, Rayleigh scattering and Mie scattering. Furthermore, the mirror reflectivity, the mirror point spread function, and the acceptances of the plexiglass panels and the light collecting funnels in front of the cameras are taken into account. See Table 2 for a summary of the efficiencies which are relevant for the simulations. In the table only the mean values averaged over the wavelength region from 300 to 600 nm are given, in the simulations the efficiencies depend on the wavelength. The point

spread functions of the telescope mirrors are extracted from the point runs. The time-resolved photon to photoelectron conversion by the PMTs is modeled using a measured PMT pulse shape and a measured single photoelectron spectrum. Finally, the trigger processes and the digitization of the PMT pulses are simulated in detail.

The simulated events are stored in the same format as the raw experimental data and are processed with the same event reconstruction and analysis chain as the experimental data. Showers induced by photons as well as by hydrogen, helium, oxygen, and iron nuclei were simulated for the zenith angles $\theta_{\rm MC} = 0°$,$20°$,$30°$, and $45°$. For the purpose of comparing the experimental data with the Monte Carlo predictions, the Monte Carlo events are weighted to generate the appropriate spectrum. The events induced by the proton, helium, oxygen, and iron nuclei are weighted according to the cosmic ray abundances of the corresponding groups from (e.g. Wiebel et al. 1998). For each type of primary particle, and for each zenith angle approximately $2 \cdot 10^5$ showers have been generated.

The excellent agreement of the observable quantities in the experimental data and the Monte Carlo data for cosmic ray-induced showers as well as for photon-induced showers is described in detail in Konopelko et al. (1998) and in Aharonian et al. (1998). The comparisons between data and Monte Carlo which are relevant for the analysis of the Mkn 501 data of this paper are discussed in the following 4 subsections.

Three different Monte Carlo event-samples have been generated, with different trigger settings and mirror point spread functions, corresponding to the three data-taking periods.

### *3.2. Data sample and data cleaning*

The analysis described in this paper is based on 110 hours of Mkn 501 data acquired between March 16th, 1997 and October 1st, 1997 under optimal weather conditions (i.e. a clear sky and a humidity less than 90%), with the optimal detector performance, and with Mkn 501 being more than $45°$ above the horizon. Only data runs where all 4 IACTs were operational and in which not more than 20 pixel were defective in any IACT have been admitted to the analysis. Furthermore the data runs had to satisfy the requirements of the mean cosmic ray rate deviating by less than 15% from the zenith angle dependent expectation value, and the width parameter averaged over all events and all telescopes deviating by less than 6% from the zenith angle dependent expectation value.

The Mkn 501 data were acquired in the so called "wobble mode" (Daum et al. 1997). In this mode the telescopes are pointed into a direction which is shifted by $0.5°$ in declination with respect to the source direction. The direction of the shift is reversed for each data run of 20 minutes duration. For each run, the solid-angle region located $1°$ from the Mkn 501 location on the opposite side of the camera center is used as OFF region for estimates concerning the background contamination of the ON region by cosmic ray-induced showers. The large angular distance between the ON solid-angle region around the Mkn 501 direction and the OFF solid-angle region assures a negligible contamination of the OFF data with Mkn 501 $\gamma$-rays. The symmetric location of the ON and the OFF region in the camera with respect to the optical axis and the camera geometry assures almost equal background characteristics for both regions. The zenith angle dependence of the background rate is to first order compensated by using as many runs with lower-declination OFF regions as with higher-declination OFF regions.

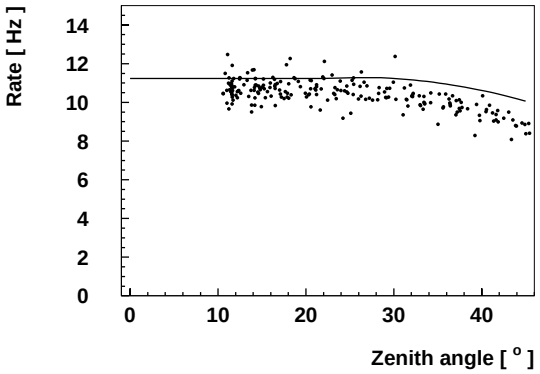


**Fig. 1.** The cosmic ray detection rate of the IACT system (dots) as a function of zenith angle (data from data-period I). Monte Carlo rate predictions are superimposed (solid line). The measured and the Monte Carlo data agree with an accuracy of 10% (hardware threshold, no cuts).

The overall stability of the detector and the understanding of the detector performance during the three data periods has been tested by comparing several key Monte Carlo predictions for hadron-induced showers with the experimental results. In the following 3 subsections tests concerning photon-induced showers, based on $\gamma$-rays from Mkn 501, will be described.

The observed cosmic ray detection rates have been compared with the detection rates as inferred from the Monte Carlo simulations together with the cosmic ray fluxes from the literature. In Fig. 1 the dependence of the cosmic ray detection rate on the zenith angle is shown for the first data-period and the corresponding Monte Carlo data-sample. The Monte Carlo describes the dependence with an accuracy of 10%. In Fig. 2 the measured and predicted rates are shown for the whole 1997 data-base. The measured rates have been normalized to a zenith angle of $15°$ according to the empirical parameterization shown in Fig. 1. For all three data periods the Monte Carlo simulations predict the measured rates with an accuracy of 10%, and they accurately describe the relative rate differences between the data-taking periods. The measured rates within each data-period show a spread of $4\%$ FWHM, after correcting for the zenith angle dependence of the rate. The origin of this small spread is still unclear. The rate deviations do not correlate with the temperature, the pressure, or the humidity, as measured at the Nordic Optical Telescope which is localized within several hundred meters from the HEGRA site. Neither is a correlation found with the V-band extinction measured with the Carlsberg Meridian Circle which is situated at a distance of $\sim$500 m from the HEGRA site.

To summarize, the measurements of the cosmic-ray event rate prove the stability of the IACT system at a level of 5%

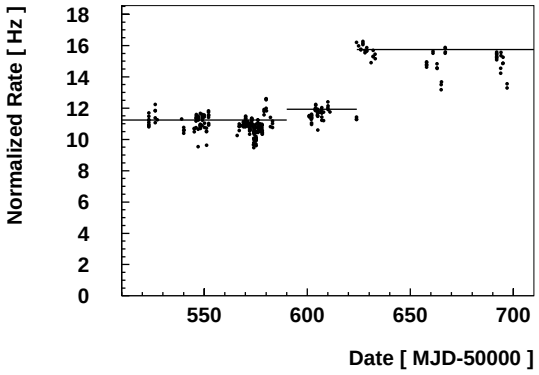


**Fig. 2.** The measured cosmic ray detection rate (dots) and the Monte Carlo based predictions (solid line) are shown for all the cosmic ray data of the Mkn 501 runs of 1997. The measured rates have been normalized to a zenith angle of 15° using an empirical parameterization. The Monte Carlo simulations for 0° zenith angle have been used (hardware threshold, no cuts).

and the event rate is correctly predicted by the Monte Carlo simulations using the cosmic ray abundances from the literature with an accuracy of 10%.

### *3.3. The stereoscopic reconstruction of the direction of primary particles*

Based on the stereoscopic images of the shower, the shower axis is reconstructed accurately and unambiguously using a simple geometric method (Aharonian et al. 1997b). The reconstruction permits to determine the distances of the telescopes from the shower axis and consequently, to accurately reconstruct the shower energy and to efficiently suppress the background of cosmic ray-induced showers.

The reconstruction method uses the standard second moment parameterization (Hillas 1985; Fegan 1996) of the individual images. Each image is described by an ellipsoid of inertia computed from the measured Cherenkov light intensities in the camera. The intersection of the major axes of *two images* superimposed in the "common focal plane", i.e. in directional space, yields *one* estimate of the shower direction. If more than two telescopes observed a shower, the arrival directions computed for all pairs of images are combined with a proper weighting factor to yield the common estimate of the arrival direction. The weighting factor is chosen proportional to $\sin\,\delta$, where $\delta$ is the angle between the two major axes. Taking into account the shower direction, the shower core is reconstructed using a very similar geometric procedure. Note, that this method is based exclusively on the geometry of the imaging systems and of the shower axis and does not rely on any Monte Carlo predictions.

The angular resolution achieved with this method has been determined using both Mkn 501 $\gamma$-ray data and the Monte Carlo simulations. In the case of the Mkn 501 data this is done as follows. The squares of the angular distances $\Theta$ of the reconstructed shower directions from the Mkn 501 position are histogrammed. The subtraction of the corresponding distribution of the fictitious OFF source yields the background-subtracted distribution of the $\gamma$-ray events. In order to reduce the background-induced fluctuations, the analysis is performed with the $\gamma$/h-separation cut $\bar{w}_{\rm sc} < 1.3$ (see next subsection for the definition of $\bar{w}_{\rm sc}$). In the following, the Monte Carlo photon-induced showers are weighted according to a power law spectrum with differential spectral index of $-2.2$.

On the left side of Fig. 3 the $\Theta^2$-distributions for the ON and the OFF regions are shown for the zenith angle interval 0°-30°. On the right side of Fig. 3 the distribution obtained after background subtraction is compared to the distribution for the 20° Monte Carlo showers. There is good agreement between the data and the Monte Carlo. The projected angular resolution is 0.1° for showers near the zenith and is slightly worse for the 30°- and the 45°-showers i.e. 0.11° and 0.12° respectively. In the analysis presented in this paper, only a loose cut of $\Theta < 0.22°$ is used which accepts, after softwarethreshold, 85% of the photon induced showers and rejects 99% of the hadron-induced showers. By this loose cut the systematic uncertainties caused by the energy-dependent $\gamma$-ray acceptance of the cut are minimized.

In Fig. 4 the $\gamma$-ray acceptance ($\kappa_{\gamma,\Theta}$) of the angular cut is shown as a function of the reconstructed shower energy, as determined both from the Mkn 501 and from Monte Carlo data. In the case of the Mkn 501 data the same background subtraction technique is used as described above. For the lowest energies ($< 1$ TeV) the $\gamma$-ray acceptance is slightly lower than for higher energies, i.e. the angular resolution is slightly worse. This is a consequence of the photon statistics per image and the corresponding uncertainty of the images' major axes. At higher energies the angular resolution improves less than expected from the increase in photon statistics. This is a consequence of an increasing fraction of showers which at higher energies are still able to fulfill the trigger criteria, albeit having impact points far away from the telescope system. With increasing distance of the impact point from the telescope system, the accuracy of the direction reconstruction decreases as a consequence of smaller angles between the image axes of the different telescopes.

### *3.4. Image analysis gamma/hadron separation*

The IACT technique permits the suppression of the background of cosmic ray-induced showers by the directional information and, additionally, by analysis of the shapes of the shower images. In the case of stereoscopic IACT systems, the gamma/hadron separation power of the parameter $WIDTH$ of the standard second moment analysis, which describes the transverse extension of the shower image in one camera, can be increased substantially, due to two facts: First, the location and the orientation of the shower axis is known from the three-dimensional event reconstruction and cuts can be optimized accordingly. Second, a telescope system provides complementary information about the transversal extension of the shower obtained from different viewing angles.

The parameter "mean scaled width" $\bar{w}_{\rm sc}$ (Konopelko 1995; Daum et al. 1997) has been used for gamma/hadron-separation. It is defined according to:

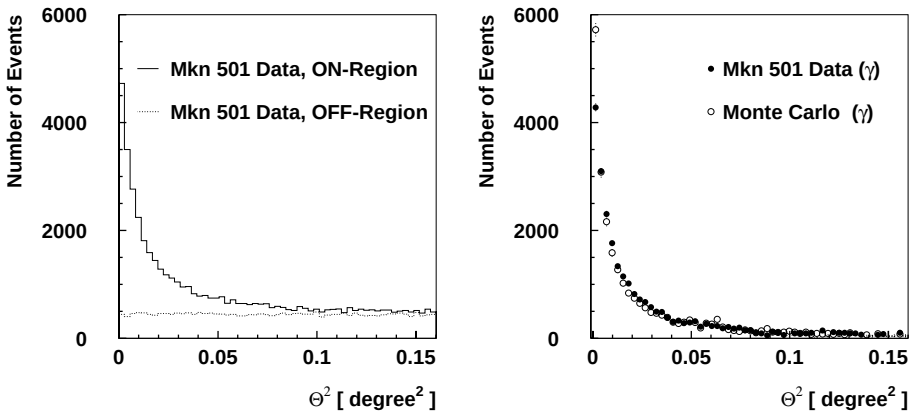


**Fig. 3.** On the left side, the squared angular distances $\Theta^2$ of the reconstructed event directions from the Mkn 501 direction (full line) and from the OFF source direction (dotted line) are shown for zenith angles below $30^\circ$. On the right side, the measured background subtracted $\Theta^2$-distribution (full circles) is compared to the $20^\circ$ zenith angle Monte Carlo simulations (open circles) All distributions have been computed using the software threshold of at least 2 IACTs with $size > 40$ and the loose $\gamma$/h-separation cut $\bar{w}_{sc} < 1.3$.

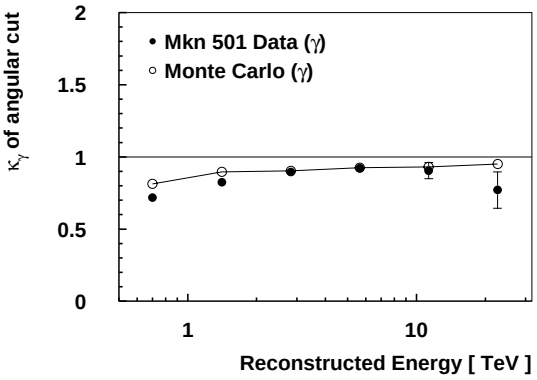


**Fig. 4.** The $\gamma$-ray acceptance of the cut $\Theta < 0.22^\circ$ as a function of the reconstructed primary energy, computed with the Mkn 501 gamma-rays (full circles) and with the Monte Carlo simulations (open circles). The computation of the cut acceptances is based on the number of excess events found in the ON region of angular radius of $0.45^\circ$ (cuts as in Fig. 3).

$$\bar{w}_{\rm sc} \;=\; \frac{1}{N_{\rm tel}} \sum_i \frac{WIDTH_i}{\langle WIDTH(r_i, size_i, \theta)\rangle_\gamma}, \qquad (1)$$

where the sum runs over all $N_{tel}$ telescopes which triggered. $WIDTH_i$ is the $WIDTH$-parameter measured with telescope $i$ and $\langle WIDTH(r_i, size_i, \theta)\rangle_\gamma$ is the $WIDTH$-value expected for photon-induced showers, given the telescope distance $r_i$ from the shower axis, the total number of photoelectrons, $size_i$, observed in the telescope, and the zenith angle $\theta$ of observations. The $\langle WIDTH(r_i, size_i, \theta)\rangle_\gamma$-values are computed from a Monte Carlo table, using an empirical function for interpolation between the simulated zenith angles. By using a *scaled* $WIDTH$-parameter, it is possible to take into account that on average the widths of the shower images widen with increasing telescope distance from the shower axis and with the total number of photoelectrons recorded in a telescope. By *averaging* over the values computed for each telescope, the statistical accuracy of the parameter determination improves *and* the information about the shower gained from different viewing angles is combined.

Fig. 5 shows the distribution of the $\bar{w}_{\rm sc}$ parameter for the Mkn 501 $\gamma$-rays and for the Monte Carlo photon data-sample. The distribution for the Mkn 501 $\gamma$-rays has been obtained as follows. The $\bar{w}_{\rm sc}$-values of the events satisfying the loose cut on the angular distance $\Theta$ from the Mkn 501 location $\Theta < 0.3^\circ$ are histogrammed. The subtraction of the corresponding OFF distribution yields the background-free distribution of the $\gamma$-ray events. As can be seen in Fig. 5 the experimental distribution and the Monte Carlo distribution are in excellent agreement.

In the analysis of this paper only a loose cut of $\bar{w}_{\rm sc} < 1.2$ which accepts, after softwarethreshold, 96% of the photons and rejects 80% of the cosmic ray-induced air showers is used. With this loose cut the systematic uncertainties caused by the energy dependent $\gamma$-ray acceptance of the cut are minimized. In Fig. 6 the $\gamma$-ray acceptances $\kappa_{\gamma,\rm img}$ of the shape cut as determined from data and as determined from Monte Carlo as a function of the reconstructed energy are compared to each other. The results are in excellent agreement with each other. Due to background fluctuations, the determination of the cut acceptance from experimental data can yield values larger than one.

### *3.5. Reconstruction of the primary energy and determination of differential spectra*

The determination of a differential $\gamma$-ray spectrum is performed in several steps. In the first step, for all events of the ON and the OFF region the primary energy $E$ is reconstructed under the assumption that the primary particles are all photons. The reconstruction is based on the fact that, for a certain type of primary particle and a certain zenith angle $\theta$, the density of atmospheric Cherenkov light created by the extensive air shower at a certain distance from the shower axis is to good approximation proportional to the energy of the primary particle. Presently two algorithms are used:

1. The first method is based on the functions $\langle size(r, E, \theta)\rangle_\gamma$ and
$\sigma_{size}(r, E, \theta)^2 \equiv \left\langle \left( size(r, E, \theta) - \langle size(r, E, \theta)\rangle_\gamma \right)^2 \right\rangle_\gamma$
which describe the expected sum of photoelectrons, $size$, and its variance as a function of the distance $r$ of a telescope from the shower axis, the primary energy $E$ of the photon, and the zenith angle $\theta$. Both functions are computed from the Monte Carlo event-sample and are tabulated in $r$-, $E$-, and $\theta$-bins. Given, for the $i$th telescope, the shower axis dis-

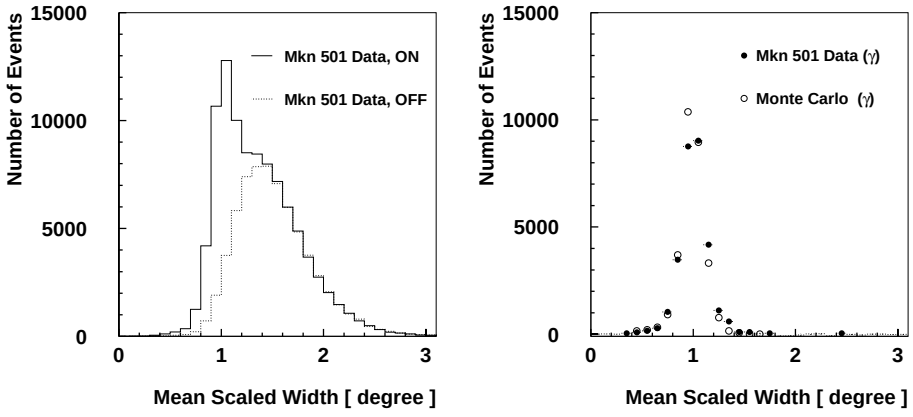


**Fig. 5.** On the left side, the mean scaled width distribution is shown for the ON region (full line) and for the OFF region (dotted line). On the right side, the background subtracted distribution (full circles) is compared to the Monte Carlo distribution (open circles). (all distributions: software threshold: at least 2 IACTs with $size > 40$, and, cut: $\Theta < 0.3^\circ$, data: all zenith angles, Monte Carlo: zenith angle = 20°).

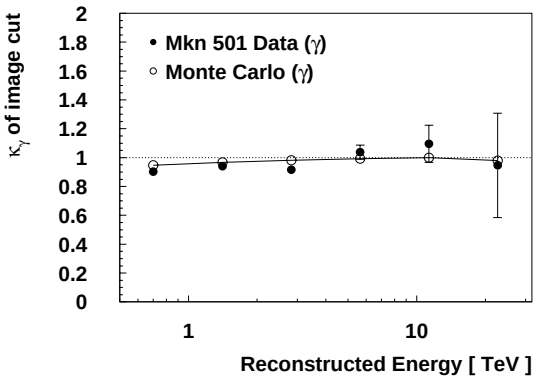


**Fig. 6.** The $\gamma$-ray acceptance of the cut $\bar{w}_{\rm sc} < 1.2$ as a function of the reconstructed primary energy, computed with the Mkn 501 gamma-rays (full circles) and with the Monte Carlo simulations (open circles) (cuts as in Fig. 5).

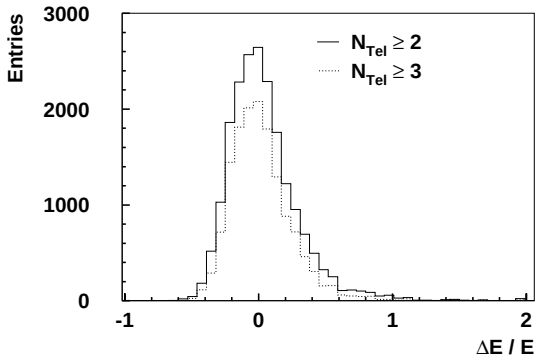


**Fig. 7.** The relative error of the energy reconstruction $\Delta E / E$ (with $\Delta E > 0$ if the reconstructed energy is higher than the true energy), shown for $\gamma$-ray induced showers. The full line shows the distribution for all showers with at least 2 telescopes with $size > 40$ and the dotted line shows the distribution for all showers with at least 3 telescopes with $size > 40$ (Monte Carlo, zenith angle 20°, after loose $\gamma$/h-separation cuts, weighting according to $\mathrm{d}N_\gamma / \mathrm{d}E \propto E^{-2.2}$).

tance $r_i$ from the stereoscopic event analysis and the sum of recorded photoelectrons $size_i$, an estimate $E_i$ of the primary energy is made by numerical inversion of the function $\langle size(r, E, \theta)\rangle_\gamma$. Subsequently the energy estimates from all triggered telescopes are combined with a proper weighting factor proportional to $1/(\sigma_{size}(r_i, E_i, \theta))^2$ to yield a common energy value.

2. In a very similar approach $E$ is estimated from the $size_i$ and the $r_i$ using a Maximum Likelihood Method which takes the full probability density functions (PDFs) $p(size; r, E, \theta)$ of the $size$-observable into account. The PDFs are determined from the Monte Carlo-simulations for certain bins in $r$, $E$, and $\theta$. The common estimate for the energy $E$ maximizes the joint a posteriori probability function $\prod_i p(size_i; r_i, E, \theta)$ that the $size_i$-values have been observed at the zenith angle $\theta$ and at the distances $r_i$.

Monte Carlo showers have been simulated for the 4 discrete zenith angles $0^\circ$, $20^\circ$, $30^\circ$, and $45^\circ$. The energies for arbitrary $\theta$-values between 0° and 45° are determined by interpolation of the two energy estimates computed with the Monte Carlo tables of the adjacent zenith angle values below and above $\theta$. Hereby an interpolation linear in $\cos(\theta)^{-\zeta}$ is used, where $\zeta = 2.4$ is derived as described below. Very small images with $size < 40$ are excluded from the analysis. Both methods yield the same energy reconstruction accuracy of $\Delta E/E \sim 20\%$ for photon-induced showers, almost independent of the primary energy. In the analysis presented below the Maximum Likelihood Method is used. In Fig. 7 the relative reconstruction error $\Delta E / E$ is shown for the second method for all triggered $\gamma$-ray showers which pass the loose $\gamma$/h separation cuts and which produce at least two or three images with $size > 40$. Increasing the requirement on the minimum number of images improves the energy resolution slightly but reduces the $\gamma$-ray statistics. In the following we are interested in one-day spectra with sparse photon statistics; consequently we will use the weaker condition of only two telescopes with $size > 40$.

In the second step, the differential photon flux per energy channel is computed using the formula

$$\frac{\mathrm{d}\Phi}{\mathrm{d}E}(E_i) = \frac{1}{\Delta t\, \Delta E_i}$$
$$\left\{ \sum_{j=1}^{n_{\mathrm{on},i}} \left[\kappa_{\gamma,\Theta}(E_j, \theta_j)\, \kappa_{\gamma,\mathrm{img}}(E_j, \theta_j)\, A'_{\mathrm{eff}}(E_j, \theta_j)\right]^{-1} -\right.$$

$$\left. \sum_{j=1}^{n_{\mathrm{off},i}} [\kappa_{\gamma,\Theta}(E_j,\theta_j)\,\kappa_{\gamma,\mathrm{img}}(E_j,\theta_j)\,A'_{\mathrm{eff}}(E_j,\theta_j)]^{-1} \right\} \quad (2)$$

where $\Delta t$ is the observation time and $\Delta E_i$ is the width of the $i$th energy bin. The first sum runs over all ON events reconstructed in the $i$th energy bin. The second sum runs over all OFF events reconstructed in the $i$th energy bin. $E_j$ is the reconstructed energy of the $j$th event and the parameter $\theta_j$ is the zenith angle under which the source was observed when the $j$th event was recorded. The second term subtracts on a statistical basis the background contamination of the ON region. The effective area $A'_{\mathrm{eff}}$ accounts for the acceptance of the detector *and* its energy resolution. The factors $\kappa_{\gamma,\Theta}$ and $\kappa_{\gamma,\mathrm{img}}$ account for the $\gamma$-ray acceptances of the angular cut and the image cut, respectively. Given the differentail flux, the integral flux can be computed easily by integrating Eq. 2 over the relevant energy range.

Generally, the effective area is computed from

$$A_{\mathrm{eff}}(E,\theta) \;=\; \frac{N_{tr}(E,\theta)}{N_{\mathrm{MC}}(E,\theta)}\,A_{\mathrm{MC}}(E,\theta) \quad (3)$$

where $N_{\mathrm{MC}}$ is the number of Monte Carlo $\gamma$-ray-induced showers generated for a certain energy and zenith angle bin, $N_{tr}$ is the number of these showers which trigger the detector and pass the selection cuts, and $A_{\mathrm{MC}}$ is the area over which the Monte Carlo showers were thrown. The area $A_{\mathrm{MC}}$ is chosen sufficiently large (depending on the primary energy and the simulated zenith angle between $2 \times 10^5$ and $6 \times 10^5\,\mathrm{m}^2$), so that virtually no exterior events trigger the experiment.

The energy resolution of the detector is taken into account by using a slightly modified effective area $A'_{\mathrm{eff},\alpha}$ which takes, for a given power law spectrum $\Phi(E) \propto E^{\alpha}$, the response function of the energy reconstruction $p(E,\tilde{E})$ (properly normalized) into account:

$$A'_{\mathrm{eff},\alpha}(\tilde{E};\theta) \;=\; \frac{\int dE\; p(E,\tilde{E};\theta)\; A_{\mathrm{eff}}(E,\theta)\; \Phi(E)}{\Phi(\tilde{E})}. \quad (4)$$

In practice, $A'_{\mathrm{eff},\alpha}$ is computed with Eq. 3, weighting the events according to an incident power law spectrum with differential spectral index $\alpha$ and using for $E$ the reconstructed energy and not the true energy. Hereby the cut on the distance $r$ of the shower axis from the center of the telescope system $r < 195\,\mathrm{m}$ which is also used in the spectral analysis is taken into account.

Eq. 2 permits, by definition, to reconstruct accurately a differential power law spectrum with index $\alpha$. Due to the good energy resolution of 20% of the IACT system, $A'_{\mathrm{eff},\alpha}$ depends only slightly on $\alpha$. Monte Carlo studies prove that power law spectra with spectral indices between $-1.5$ and $-3$ are reconstructed with a systematic error smaller than 0.1 using $A'_{\mathrm{eff},\,\alpha}$ with a fixed value of $\alpha = -2.2$. Furthermore we have tested this method with several other types of primary spectra, i.e. with broken power law spectra and with power law spectra with exponential cut-offs. The method, used with $A'_{\mathrm{eff},\,-2.2}$, reproduces the input-spectra with good accuracy.

Differential Mkn 501 spectra obtained with this method, as well as the method for fitting model spectra to the data, will be discussed below. Alternatively we have tested the standard forward folding technique and more sophisticated deconvolution methods. The deconvolution methods yield a slightly improved effective energy resolution at the expense of a heavier use of detailed Monte Carlo predictions and/or a larger statistical error of the individual differential flux estimates.

On the left side of Fig. 8, $A_{\mathrm{eff}}(E,\theta)$ and on the left side of Fig. 9, $A'_{\mathrm{eff}}(E,\theta)$ are shown, computed for $\theta_{\mathrm{MC}} = 0^\circ,\ 20^\circ,\ 30^\circ$, and $45^\circ$. The zenith angle dependence of the $A_{\mathrm{eff}}$-curves can be described with the following empirical formula:

$$A_{\mathrm{eff}}(E,\theta) \;=\; \frac{1}{\cos^{\xi}(\theta)}\,A_{\mathrm{eff}}(\cos^{\zeta}(\theta)\;\cdot\;E, 0^\circ) \quad (5)$$

with $\xi = 1.7$ and $\zeta = 2.4$ (see Fig. 8, right side). The same formula with the exponents $\xi = 0.4$ and $\zeta = 2.2$ describes the zenith angle dependence of the $A'_{\mathrm{eff}}$-curves (see Fig. 9, right side). This formula is used in the data analysis to interpolate $A_{\mathrm{eff}}$ between the simulated zenith angles.

The Monte Carlo reproduces nicely the following properties of $\gamma$-ray-induced showers:

- the shape of the lateral Cherenkov light distribution as a function of the primary energy (Aharonian et al. 1998),
- the single telescope trigger probability as function of shower axis distance and primary energy, and
- the distribution of the shower cores,

all determined with the Mkn 501 $\gamma$-ray data-sample. Hence, we are confident that the Monte Carlo correctly predicts the $\gamma$-ray effective areas, except for a possible scaling factor $a = 1.00 \pm 0.15$ in the energy which derives from the accuracies with which the atmospheric absorption and the Cherenkov photon to ADC counts conversion factor are known. Note, that the possible scaling factor $a$ introduces an uncertainty in the absolute flux estimates, but not in the measured differential spectral indices.

The Crab Nebula is known to be a TeV source with an approximately constant TeV emission (Buckley et al. 1996). We have tested the full analysis chain described above and the stability of the IACT system directly with $\gamma$-rays from this source. Within statistical errors the Crab observations prove that the IACT system runs stably and that the analysis based on the Monte Carlo simulations accounts correctly for the hardware changes performed during 1997 as well as for the IACT system's zenith angle dependence of the $\gamma$-ray acceptance (Aharonian et al. 1999 in preparation).

## 4. The 1997 Mkn 501 light curve

Between March 16th and October 1st, 1997, 110 h of Mkn 501 data, satisfying the conditions described above, were acquired. The excess of about $38,000$ photons is shown in Fig. 10 in equatorial coordinates (hardware threshold, no cuts). Note, that the figure shows the number of excess events as function of declination and right ascension and not a likelihood contour. The mean location of the excess photons coincides with the Mkn 501 location with an accuracy of $0.01^\circ$ (Pühlhofer et al. 1997), corresponding to an angular resolution of the IACT system of better

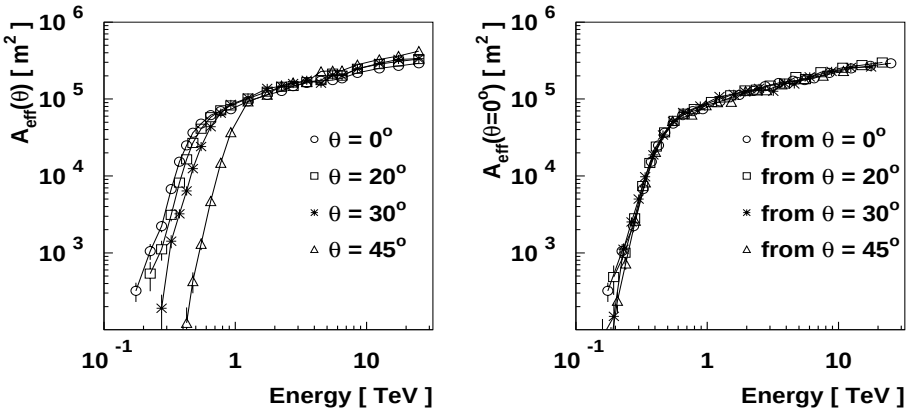


**Fig. 8.** On the *left side* the effective areas of the HEGRA system of 4 IACTs for $\gamma$-ray detection as functions of the primary energy are shown for the 4 different zenith angles $\theta = 0^\circ$, $20^\circ$, $30^\circ$, and $45^\circ$ (Monte Carlo). The *right side* shows the effective area for vertically incident showers $\theta = 0^\circ$ calculated with the effective areas at the zenith angles $\theta = 20^\circ$, $30^\circ$, and $45^\circ$ according to Eq. 5 (hardware threshold of at least 2 triggered telescopes, no cuts).

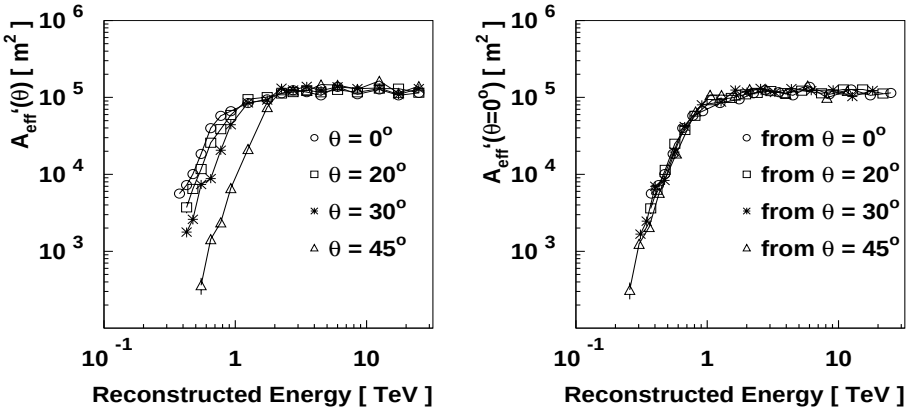


**Fig. 9.** On the *left side* the effective areas as function of the *reconstructed* primary energy are shown for the 4 different zenith angles (Monte Carlo). The same cuts as in the spectral studies have been used, i.e. the software threshold of two telescopes with a $size$-value above 40 and a distance of the shower axis from the center of the telescope system smaller than 195 m. On the *right side* it is shown, how the effective area for vertically incident showers can be computed from the effective areas computed for the other three zenith angles using Eq. 5.

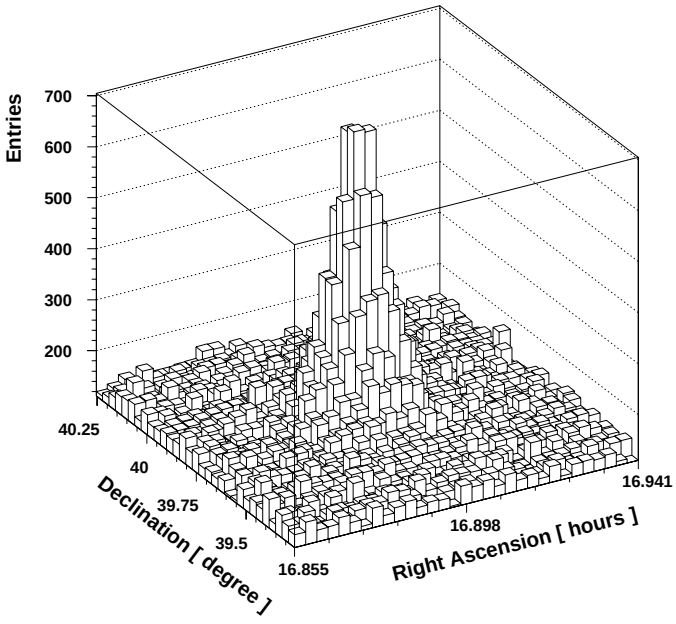


**Fig. 10.** All events reconstructed in the $1^\circ \times 1^\circ$ solid-angle region centered on the Mkn 501 direction. The prominent $\gamma$-ray excess can be seen above the approximately flat background (hardware threshold, no cuts).

than 40 arc sec when limited by systematic uncertainties and not by statistics.

Fig. 11 shows the differential spectra obtained for 8 exemplary individual nights. For each of the four data periods March/April, April/May, May/June, and June/July 1997 a night of weak emission and a night of strong emission has been chosen. As can be seen, the stereoscopic IACT system, due to its high signal to noise ratio and due to an energy resolution of $20\%$, permits a detailed spectral analysis on a diurnal basis. The spectra can approximately be described by power law models, although above 5 TeV the spectra apparently steepen (see also Aharonian et al. 1997c; Samuelson et al. 1998).

In a first analysis, we fit the data with power laws in the energy region from 1 to 5 TeV. The lower bound of the fit region is determined by the requirement of the bound being higher than the energy threshold of the IACT system in the zenith angle interval from 0° to 45°. The upper bound of 5 TeV has been chosen to minimize systematic correlations between the emission intensity and the fitted spectral index which could be caused by the combined effect of a curvature of the Mkn 501 spectrum and the effective maximum fit range. The latter actually is smaller for nights of low Mkn 501 activity, since for these nights the higher energy channels above $\sim 5$ TeV are frequently not populated and do not contribute to the fit result.

In order to minimize the correlations between the fitted flux amplitude and the spectral index due to the fitting procedure, the model $\mathrm{d}\Phi/\mathrm{d}E = \Phi_{2\,\mathrm{TeV}} \cdot (E\,/\,2\,\mathrm{TeV})^{\,\alpha}$ is used, where $\Phi_{2\,\mathrm{TeV}}$ is the differential flux at 2 TeV and $\alpha$ is the spectral index.

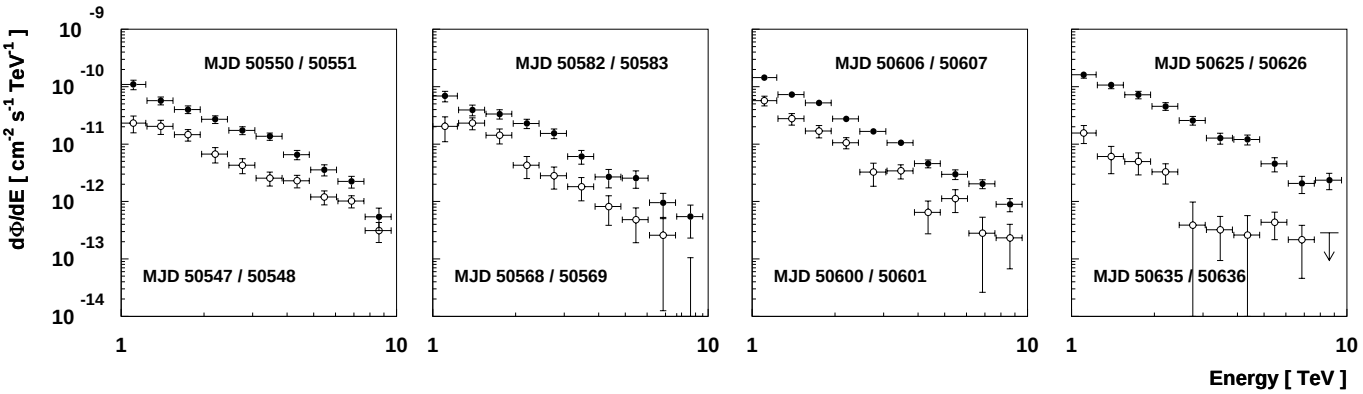


**Fig. 11.** The differential $\gamma$-ray spectra of eight individual nights. For each of the four data periods March/April, April/May, May/June, and June/July, 1997 a night of weak emission and a night of strong emission has been chosen. Statistical errors only; see text for systematic errors; the upper limit has $2\sigma$ confidence level (MJD 50550 corresponds to April 12th, 1997).

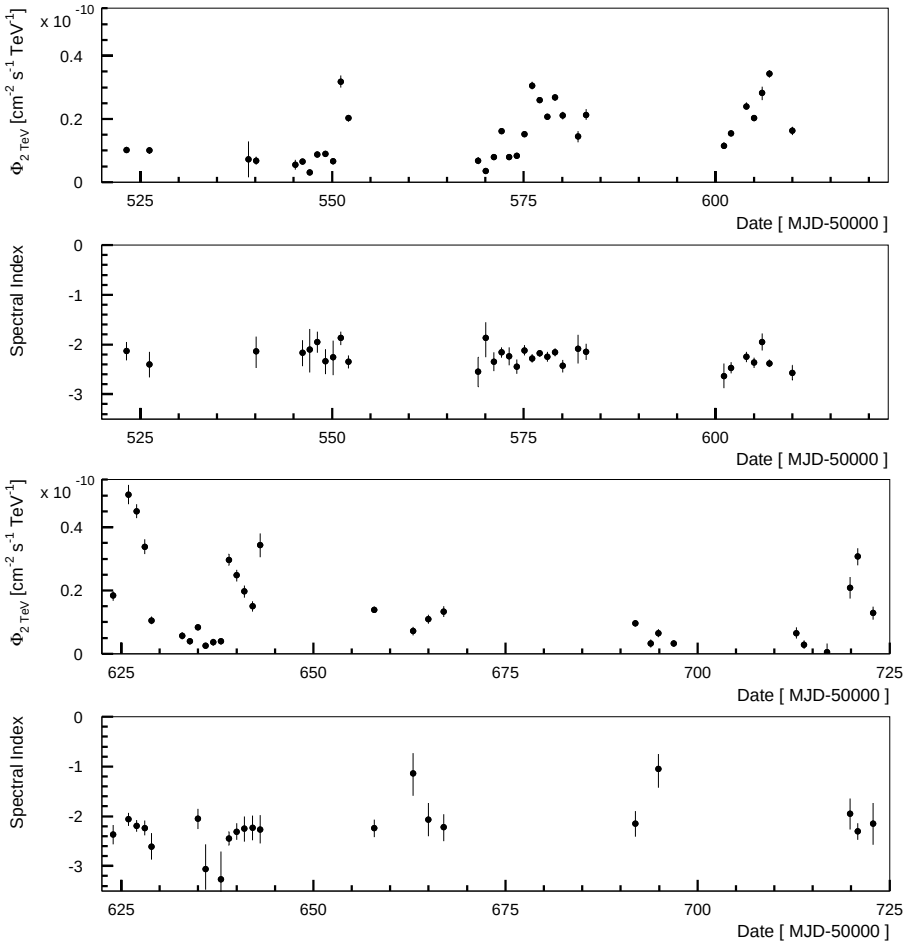


**Fig. 12.** Daily flux amplitudes $\Phi_{2\,\mathrm{TeV}}$ and differential spectral indices (1-5 TeV) for the 1997 Mkn 501 data. For clearness, spectral indices are shown only for the days with sufficient statistics, i.e. with errors on the spectral index smaller than 0.5. Statistical errors only; see text for systematic errors (MJD 50550 corresponds to April 12th, 1997).

The energy 2 TeV approximately equals the median energy of the Mkn 501 $\gamma$-rays recorded with the IACT system.

We estimate the systematic error on the flux amplitude to be $\simeq$20%. This error is dominated by the 15% uncertainty of the energy scale. The systematic error on the spectral index is currently estimated to be 0.1 and derives from the Monte Carlo-dependence of the results. The systematic errors as well as more detailed studies of the differential Mkn 501 spectra, especially in the energy range below 1 TeV and above 10 TeV, will extensively be discussed in a forthcoming paper. Note, that all errors shown in the following plots are statistical only.

The differential fluxes at 2 TeV and the spectral indices determined on a daily basis are shown in Fig. 12. In Table 3 the results are summarized. The gaps in the light curve are caused

**Table 3.** Results on diurnal basis. Statistical Errors only; see text for systematic errors.

| Start[a] | $\Delta t$ [b] | $\mathrm{d}\Phi/\mathrm{d}E\,(2\,\mathrm{TeV})$[c] | Spectral index[d] | $\Phi(>1\,\mathrm{TeV})$[e] |
|---|---|---|---|---|
| 50523.1266 | 2.42 | 10.22 +0.96 −0.88 | −2.13 +0.18 −0.19 | 35.55 ± 3.74 |
| 50526.1791 | 1.35 | 10.01 +1.05 −1.13 | −2.40 +0.25 −0.26 | 36.73 ± 4.14 |
| 50527.2305 | 0.32 | – | – | 5.96 ± 8.09 |
| 50539.0783 | 0.32 | 7.21 +5.63 −5.65 | −3.48 +3.13 −1.52 | 13.41 ± 10.02 |
| 50540.0758 | 1.21 | 6.79 +1.33 −1.28 | −2.14 +0.30 −0.33 | 24.39 ± 5.19 |
| 50545.2038 | 0.56 | 5.51 +1.56 −1.58 | −2.52 +0.98 −0.68 | 19.21 ± 5.40 |
| 50546.0839 | 2.16 | 6.53 +0.83 −0.85 | −2.17 +0.26 −0.27 | 22.21 ± 3.16 |
| 50547.0566 | 2.68 | 3.16 +0.73 −0.70 | −2.10 +0.41 −0.46 | 11.06 ± 2.63 |
| 50548.0537 | 2.63 | 8.71 +0.91 −0.83 | −1.95 +0.21 −0.22 | 32.79 ± 3.31 |
| 50549.0512 | 2.88 | 8.89 +0.93 −0.84 | −2.34 +0.24 −0.25 | 34.55 ± 3.89 |
| 50550.0561 | 1.75 | 6.66 +1.00 −1.04 | −2.26 +0.34 −0.36 | 24.07 ± 3.80 |
| 50551.0671 | 1.30 | 31.76 +1.95 −1.84 | −1.87 +0.13 −0.14 | 111.99 ± 7.22 |
| 50552.0751 | 2.27 | 20.30 +1.04 −1.18 | −2.35 +0.13 −0.13 | 73.99 ± 4.16 |
| 50566.0047 | 0.16 | – | – | 6.47 ± 15.75 |
| 50567.0018 | 1.05 | – | – | 16.14 ± 5.07 |
| 50568.0608 | 0.40 | – | – | 15.20 ± 7.26 |
| 50569.0386 | 1.62 | 6.79 +0.94 −0.94 | −2.55 +0.29 −0.30 | 25.38 ± 3.65 |
| 50569.9936 | 3.17 | 3.49 +0.64 −0.63 | −1.87 +0.32 −0.39 | 11.94 ± 2.73 |
| 50570.9909 | 4.08 | 7.89 +0.65 −0.60 | −2.35 +0.19 −0.19 | 27.88 ± 2.47 |
| 50571.9882 | 4.65 | 16.15 +0.66 −0.63 | −2.16 +0.10 −0.11 | 57.39 ± 2.80 |
| 50572.9855 | 3.68 | 7.89 +0.65 −0.68 | −2.24 +0.18 −0.18 | 27.42 ± 2.56 |
| 50573.9829 | 4.84 | 8.29 +0.51 −0.56 | −2.45 +0.15 −0.14 | 31.70 ± 2.20 |
| 50575.0000 | 4.53 | 15.21 +0.78 −0.59 | −2.12 +0.11 −0.10 | 54.08 ± 2.70 |
| 50576.0015 | 2.59 | 30.52 +1.24 −1.19 | −2.28 +0.09 −0.09 | 109.59 ± 4.78 |
| 50576.9745 | 4.80 | 26.03 +0.79 −0.77 | −2.18 +0.07 −0.07 | 92.66 ± 3.34 |
| 50577.9720 | 4.00 | 20.71 +0.63 −1.00 | −2.25 +0.10 −0.10 | 74.21 ± 3.36 |
| 50578.9799 | 3.57 | 26.82 +0.81 −1.05 | −2.16 +0.08 −0.08 | 95.76 ± 3.96 |
| 50580.0128 | 2.24 | 21.12 +1.08 −1.22 | −2.43 +0.12 −0.13 | 78.77 ± 4.45 |
| 50582.0693 | 0.65 | 14.47 +1.67 −1.88 | −2.09 +0.28 −0.29 | 51.45 ± 6.64 |
| 50583.0979 | 0.79 | 21.33 +1.77 −1.63 | −2.15 +0.16 −0.16 | 79.02 ± 6.16 |
| 50601.0393 | 1.30 | 11.51 +1.08 −1.09 | −2.64 +0.26 −0.24 | 42.92 ± 4.17 |
| 50601.9731 | 2.96 | 15.52 +0.79 −0.75 | −2.47 +0.11 −0.11 | 57.10 ± 2.91 |
| 50603.9630 | 2.01 | 24.04 +1.23 −0.94 | −2.25 +0.10 −0.11 | 87.11 ± 4.16 |
| 50604.9625 | 2.60 | 20.30 +0.82 −0.99 | −2.37 +0.10 −0.10 | 74.36 ± 3.61 |
| 50606.0659 | 0.67 | 28.19 +2.03 −2.16 | −1.95 +0.17 −0.17 | 96.24 ± 7.76 |
| 50606.9592 | 2.30 | 34.39 +1.04 −1.34 | −2.38 +0.08 −0.08 | 126.10 ± 4.59 |
| 50610.0151 | 1.34 | 16.31 +1.18 −1.25 | −2.57 +0.15 −0.15 | 60.63 ± 4.52 |
| 50623.9119 | 0.98 | 18.38 +1.33 −1.57 | −2.37 +0.19 −0.19 | 63.91 ± 5.40 |
| 50625.9323 | 0.62 | 50.20 +3.09 −2.91 | −2.06 +0.13 −0.13 | 178.07 ± 10.12 |
| 50626.9801 | 0.87 | 44.99 +2.30 −2.18 | −2.19 +0.11 −0.12 | 159.90 ± 8.54 |
| 50628.0342 | 0.65 | 33.72 +2.43 −2.27 | −2.24 +0.15 −0.14 | 123.09 ± 8.51 |
| 50628.9089 | 0.95 | 10.53 +1.22 −1.18 | −2.61 +0.27 −0.26 | 38.95 ± 4.43 |
| 50631.9110 | 0.94 | – | – | 11.83 ± 3.16 |
| 50632.9106 | 0.98 | 5.68 +1.05 −1.12 | −2.24 +0.56 −0.45 | 15.15 ± 3.10 |
| 50633.9104 | 0.95 | 3.93 +0.91 −0.93 | −2.94 +0.69 −0.52 | 17.37 ± 3.54 |
| 50634.9107 | 2.03 | 8.37 +0.78 −0.72 | −2.05 +0.20 −0.21 | 28.83 ± 2.79 |
| 50635.9088 | 2.09 | 2.54 +0.50 −0.52 | −3.06 +0.50 −0.42 | 11.19 ± 2.06 |
| 50636.9242 | 0.71 | 3.74 +0.96 −0.99 | −3.28 +0.75 −0.54 | 16.29 ± 4.08 |
| 50637.9472 | 0.65 | 3.89 +0.95 −0.95 | −3.27 +0.56 −0.43 | 19.87 ± 4.10 |
| 50638.9759 | 0.89 | 29.62 +1.82 −1.72 | −2.45 +0.14 −0.13 | 106.12 ± 6.68 |
| 50639.9962 | 0.80 | 24.77 +1.79 −1.90 | −2.31 +0.17 −0.16 | 89.15 ± 6.66 |
| 50641.0329 | 0.64 | 19.70 +1.85 −2.04 | −2.25 +0.25 −0.26 | 72.00 ± 7.52 |
| 50642.0453 | 1.06 | 15.06 +1.58 −1.69 | −2.23 +0.24 −0.25 | 52.92 ± 6.75 |
| 50643.0700 | 0.48 | 34.39 +3.60 −3.87 | −2.27 +0.29 −0.28 | 117.60 ± 14.86 |
| 50657.9012 | 1.55 | 13.91 +1.00 −1.06 | −2.24 +0.17 −0.18 | 50.27 ± 3.87 |
| 50661.0177 | 0.55 | – | – | 25.66 ± 6.73 |
| 50662.9027 | 0.83 | 7.21 +1.33 −1.42 | −1.14 +0.41 −0.45 | 23.05 ± 4.42 |
| 50664.8955 | 0.82 | 10.95 +1.39 −1.42 | −2.07 +0.34 −0.33 | 38.63 ± 4.85 |
| 50666.9129 | 0.85 | 13.36 +1.69 −1.74 | −2.22 +0.26 −0.28 | 45.21 ± 6.35 |
| 50691.8717 | 1.89 | 9.62 +1.01 −1.00 | −2.15 +0.25 −0.26 | 34.64 ± 3.76 |
| 50693.8690 | 0.95 | 3.25 +1.26 −1.24 | −2.73 +0.93 −0.76 | 13.01 ± 4.36 |
| 50694.9192 | 0.67 | 6.53 +1.28 −1.28 | −1.05 +0.30 −0.38 | 22.03 ± 6.47 |
| 50696.8962 | 1.05 | 3.29 +1.01 −1.03 | −1.70 +0.51 −0.62 | 12.50 ± 4.35 |
| 50712.8598 | 0.65 | 6.53 +1.76 −1.78 | −2.37 +0.74 −0.73 | 24.38 ± 7.22 |
| 50713.8566 | 0.90 | 2.89 +1.37 −1.38 | −2.56 +1.11 −0.90 | 9.76 ± 4.87 |
| 50716.8668 | 0.50 | 0.51 +2.71 −2.70 | −1.78 +2.27 −3.22 | 1.76 ± 6.48 |
| 50719.8476 | 0.33 | 20.91 +3.37 −3.43 | −1.95 +0.31 −0.32 | 64.65 ± 10.40 |
| 50720.8479 | 0.65 | 30.83 +2.55 −2.92 | −2.30 +0.16 −0.17 | 110.59 ± 11.05 |
| 50722.8444 | 0.64 | 12.84 +2.07 −2.11 | −2.15 +0.42 −0.42 | 48.89 ± 8.37 |

[a] MJD
[b] duration of measurement in hours
[c] in ($10^{-12}$cm$^{-1}$ s$^{-1}$ TeV$^{-1}$)
[d] fitted from 1 to 5 TeV
[e] in ($10^{-12}$cm$^{-1}$ s$^{-1}$)

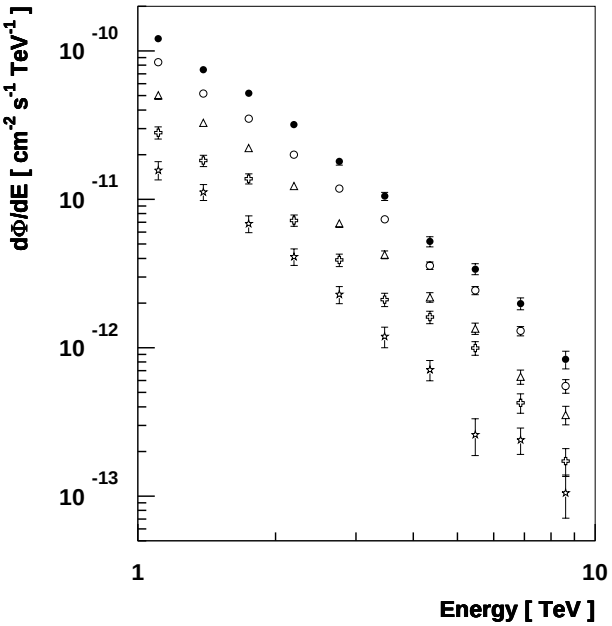


**Fig. 13.** The Mkn 501 data has been divided into 5 groups according to the activity of the source as determined on a night to night basis. For each of the 5 groups a time averaged spectrum has been determined. The five groups have (from bottom to upwards) $\Phi_{2\,\mathrm{TeV}}$ $\left[10^{-12}\,\mathrm{cm}^{-2}\,\mathrm{s}^{-1}\,\mathrm{TeV}^{-1}\right]$ of below 7, 7–10, 10–20, 20–30, and above 30, respectively. Statistical errors only; see text for systematic errors.

by the moon, since the IACT system is only operated during nights without moon. The emission amplitude is dramatically variable, the measured daily averages range from a fraction of the Crab emission to $\sim 10$ Crab, the average flux being 3 Crab. The largest flare was observed in June 1997 and peaked at June 26th/27th.

In contrast, the spectral indices are rather constant. A constant model of $\alpha = -2.25$ fits all spectral indices with a chance probability for a larger $\chi^2$ of 11%. The largest deviations have been found for the nights MJD 50550/50551 where the spectral index of $-1.87$ +0.13 $-0.14$ deviates by 2.7 $\sigma$ from the mean value and for MJD 50694/50695 where the spectral index $-1.05$ +0.30 $-0.38$ deviates by 3.2 $\sigma$ from the mean value. Henceforth, although the IACT system makes it possible to determine the daily spectral index $\alpha$ with an accuracy of $\Delta\alpha \leq 0.1$ for 15% of the nights, with an accuracy of $\Delta\alpha \leq 0.2$ for 45% of the nights, and with an accuracy of $\Delta\alpha \leq 0.35$ for 75% of the nights the evidence for a change in the spectrum is marginal.

In order to study the correlation between flux intensity and differential spectrum, we divided the IACT system data into five groups according to the diurnal emission intensity, i.e. a $\Phi_{2\,\mathrm{TeV}}$-value in units of $\left[10^{-12}\,\mathrm{cm}^{-2}\,\mathrm{s}^{-1}\,\mathrm{TeV}^{-1}\right]$ of below 7 (group i), 7–10 (group ii), 10–20 (group iii), 20–30 (group iv), and above 30 (group v), respectively. In Fig. 13 the differential spectra determined with the data of each group are shown. Within statistical errors the shapes of the five spectra are the same. This is exemplified in Fig. 14, where the four lower flux differential spectra (group i - iv) have been divided by the highest flux differential spectrum (group v). For all four cases the

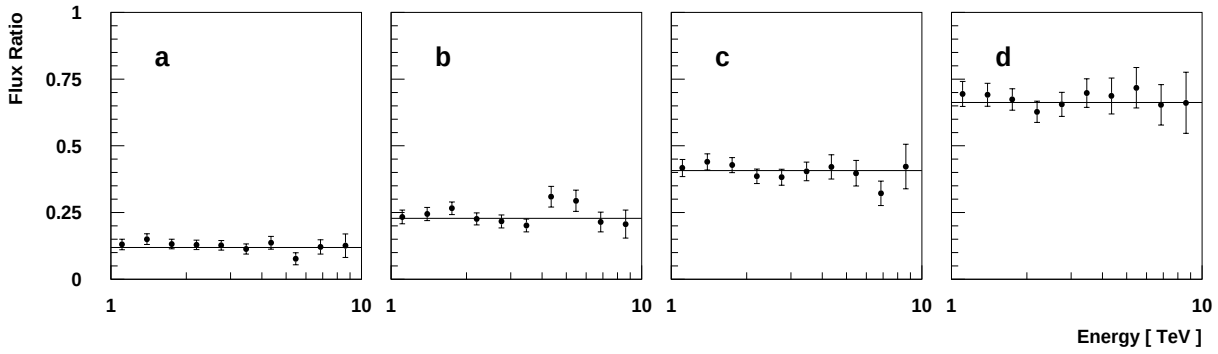


**Fig. 14a–d.** The results of dividing the differential spectra of the four lower flux intensity groups (**a**–**d** corresponding to group i-iv) by the differential spectrum of the highest flux intensity group (group v). The lines show the results of constant model fits to the ratio spectra.

ratio of the differential fluxes as a function of primary energy can be described by a constant model. The largest reduced $\chi^2$-values of a constant fit is 1.21 for 9 degrees of freedom, which corresponds to a chance probability for larger deviation from the hypothesis of a constant ratio spectrum of 28%. In Table 4 the power law spectral indices (1 to 5 TeV) of the five groups are listed. Within the statistical errors the first five indices are consistent with the mean value of $-2.25$.

We studied whether the TeV spectra during the rising epochs of the light curves systematically differ from the TeV spectra during the falling epochs of the light curves. For this purpose we selected two subsets of the data, consisting of the accumulated data where the flux increased (group vi) or decreased (group vii) by at least 25% in comparison to the preceding night. Also in this case, the ratio spectrum can well be fitted with a constant model. The reduced $\chi^2$-value of the constant model fit is 0.72 for 9 degrees of freedom, corresponding to a chance probability for larger $\chi^2$-values of 69%.

In Table 4 the power law spectral indices (1 to 5 TeV) of these two groups are given. There is only a weak indication that group vi ("rising" days) with a spectral index of $-2.19\pm0.03$ might have a flatter spectrum than group vii ("falling" days) with a spectral index of $-2.29\pm0.05$.

**Table 4.** Fit parameters of differential spectra of 7 data groups. Statistical Errors only; see text for systematic errors.

| Group | $\mathrm{d}\Phi/\mathrm{d}E\,(2\,\mathrm{TeV})$ $\left[10^{-12}/\mathrm{cm}^2\,\mathrm{s}\,\mathrm{TeV}\right]$ | Observation time [h] | Spectral index (1-5 TeV) |
|---|---|---|---|
| i | $< 7$ | 26.3 | $-2.31$ +0.10 $-0.11$ |
| ii | 7–10 | 23.6 | $-2.22$ +0.06 $-0.07$ |
| iii | 10–20 | 26.7 | $-2.27$ +0.04 $-0.05$ |
| iv | 20–30 | 25.0 | $-2.24$ +0.03 $-0.03$ |
| v | $> 30$ | 9.5 | $-2.22$ +0.04 $-0.04$ |
| vi | "rising" | 34.6 | $-2.19$ +0.03 $-0.03$ |
| vii | "falling" | 27.4 | $-2.29$ +0.05 $-0.05$ |

## 5. Study of the shortest time scales of variability

The time scales of the Mkn 501 TeV flux variability have been studied in two ways. First, the time gradients of the daily flux amplitudes $\Phi_{2\,\mathrm{TeV}}$ have been analyzed. The analysis uses the exponential increase/decay-constant $\tau$, as computed for each pair of two daily flux amplitudes according to:

$$\tau \equiv \frac{\Delta t}{\Delta\, ln\, \Phi_{2\,\mathrm{TeV}}}, \tag{6}$$

where $\Delta t$ is the time difference between the two measurements and $\Delta\, ln\, \Phi_{2\,\mathrm{TeV}}$ is the difference between the logarithms of the differential fluxes at 2 TeV. This formula has been derived by assuming a time dependence of $\Phi_{2\,\mathrm{TeV}}$ according to $\Phi_{2\,\mathrm{TeV}} \propto e^{t/\tau}$. In the case of small changes in the flux amplitude $\Delta\,\Phi_{2\,\mathrm{TeV}} \ll \bar{\Phi}_{2\,\mathrm{TeV}}$, where $\bar{\Phi}_{2\,\mathrm{TeV}}$ is the time averaged flux amplitude, the "doubling time" is commonly used to characterize the variability time scale. It is defined as the time in which the flux would have increased or decreased by 100%, assuming a linear increase or decrease of the flux:

$$t_{double} \equiv \Delta\, t\, \frac{\bar{\Phi}_{2\,\mathrm{TeV}}}{\Delta\,\Phi_{2\,\mathrm{TeV}}}. \tag{7}$$

For small changes in the flux amplitude the increase/decay-constant $\tau$ computed with Eq. 6 equals $t_{double}$ computed with Eq. 7.

In Fig. 15 the $\tau$-values computed for adjacent nights are shown. The most rapid $\tau$-values are in the order of 15 h. In Table 5 the $\tau$-values more rapid than 24 h are listed. The distribution of the $\tau$-values is to first order approximation symmetric under time reversal (see Fig. 16), i.e. the daily data does not give obvious evidence for a different rising and falling behavior.

In a second approach a dedicated search for variability on sub-day time scales has been performed. In order to search on time scales well below one hour, where the determination of a differential spectrum is plagued by large statistical uncertainties, the search directly uses the $\gamma$-ray excess rates. Using only data taken under zenith angles below 30° and applying a cut on the distance $r$ of the shower axis from the center of the telescope array $r < 200$ m, the zenith angle dependence of the $\gamma$-ray rate is negligible, i.e. less than $25\%$ for $\gamma$-ray spectra with differential spectral indices between $-2.5$ and $-1$.

In Fig. 17 the excess-rate histories computed with 10 minute temporal bins are shown for two typical nights, i.e. May 6th/7th and May 9th/10th. Here, as well as in the analysis below, the cuts $\Theta < 0.13°$ and $\bar{w}_{\mathrm{sc}} < 1.2$ have been applied. No strong

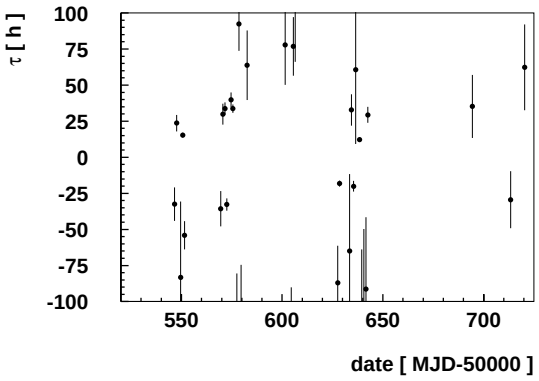


**Fig. 15.** The increase/decay constants $\tau$ computed for the flux amplitudes $\Phi_{2\,\mathrm{TeV}}$ of adjacent nights plotted against the mean MJD of the two nights (MJD 50550 corresponds to April 12th, 1997).

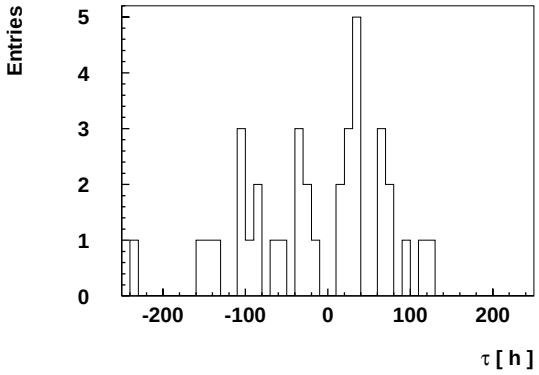


**Fig. 16.** The distribution of increase/decay constants $\tau$ computed for the flux amplitudes $\Phi_{2\,\mathrm{TeV}}$ of adjacent nights. Only $\tau$-values between $-250$ h and +250 h are shown.

**Table 5.** The most rapid increase- and decay-times.

| Night 1 [ MJD ] | Night 2 [ MJD ] | $\tau$ [ h ] |
|---|---|---|
| 50547.1 | 50548.1 | $23.6 \pm 5.8$ |
| 50550.1 | 50551.1 | $15.4 \pm 1.6$ |
| 50628.0 | 50628.9 | $-18.2 \pm 2.1$ |
| 50635.0 | 50636.0 | $-20.1 \pm 3.6$ |
| 50638.0 | 50639.0 | $12.2 \pm 1.5$ |

variability can be seen and a method is needed to decide on the statistical significance of the observed rate variations.

For the systematic search, a method introduced in (Collura & Rosner 1987) has been used. It is based on the $\chi^2$-fitting technique and permits a search on multiple time scales. It provides easy and straightforward computation of the significances of the detected variabilities. For each night a variability is searched for, using different time bin sizes, by computing the $\chi^2$-value of a constant model fit to the data, and performing an averaging procedure over the relative location of the data points within these binning schemes. We use time bins with durations $\Delta T$ between 10 minutes and 2.24 hours, i.e. with $\Delta T = (2^{n/4} \times 10\,\mathrm{minutes})$ for $n = 1$ to 15. The lower limit on the bin duration is given by the requirement of an expected number of recorded events per bin $\gtrsim 5$. The upper limit is determined by the maximum duration of the Mkn 501 observations per night which is in the order of 4 h. For each night the bin duration which yields the most significant variability detection is determined and the chance probability $p_c$ for a constant flux to yield a more significant variability is computed using an analytic approximation.

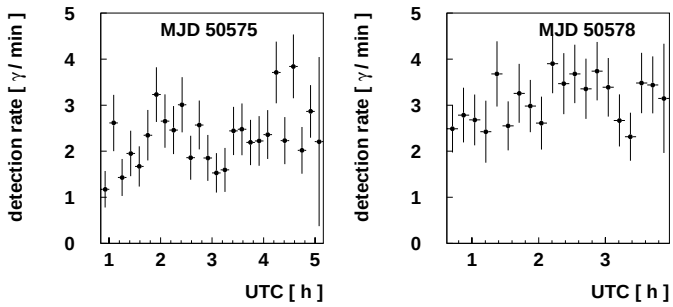


**Fig. 17.** The $\gamma$-ray detection rate of two individual nights: MJD = 50574/50575 (May 6th/7th), and 50577/50578 (May 9th/10th). A 10 minutes binning has been used.

The chance probabilities, actually the $-\log_{10}(p_c)$- values, for the 51 nights for which sufficient data with zenith angles smaller than 30° is available, are shown in Fig. 18 together with the distribution of large $-\log_{10}(p_c)$-values expected in the absence of flux variability. The $-\log_{10}(p_c)$-values distribute as expected in the absence of any variability, except for values near 0 (chance probabilities near 1) and except for values larger than 3 (chance probabilities smaller than 1 per mill). The deviation at small values derives from the analytical computation of the chance probabilities, and is thus a pure artifact of the method (see also Collura & Rosner 1987). The deviation at large values correspond to two nights, the night of May 8th/9th (MJD 50576/50577) and the night of June 7th/8th, 1997 (MJD 50606/50607), for which sub-day variability is indicated.

In the case of the first night, the most significant variability has been found with 20 minute bins; in the case of the second night with 67 min bins. The excess rates during the two nights are shown in Fig. 19. In the night from May 8th to May 9th, 1997, the $\gamma-$ray rate oscillated between 3 $\gamma$/min and 5.4 $\gamma$/min on a time scale of 1.5 hours. In the night from June 7th to June 8th, 1997, the $\gamma-$ray rate continuously increased from 4.9 $\gamma$/min to 7 $\gamma$/min within 2.6 h. The chance probability for a more significant apparent variability at constant flux is computed to be $0.8 \times 10^{-4}$ for the first night and $2.0 \times 10^{-4}$ for the second night. Taking into account that 51 nights have been searched for variability, the chance probabilities increase to 0.4% for the first night and to 1% for the second night. The variability detected in these two nights corresponds to an increase/decay constant of about 3 h for the first night and 7 h for the second night.

To summarize, the study of the time gradients of the diurnal fluxes yields smallest increase/decay times of the order of 15 h. The dedicated search for flux variability within individual nights on time scales between 10 minutes and several hours yielded weak evidence for variability on time scales of around 5 hours.

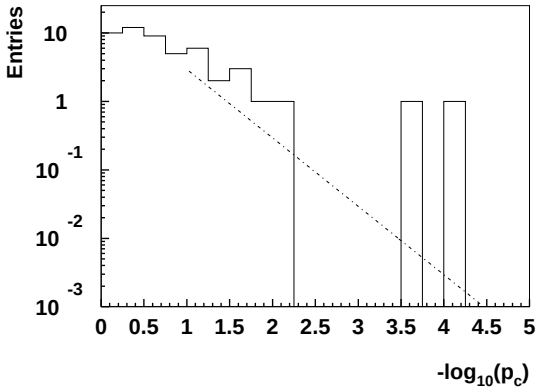


**Fig. 18.** The results of the search for sub-day variability. For each night, the chance probability $p_c$, computed with an analytic approximation, with which a constant signal would yield a more significant variability as the observed one has been computed. Shown is the distribution of the $-\log_{10}(p_c)$-values (histogram) together with distribution expected for small chance probabilities in the absence of variability (dotted line).

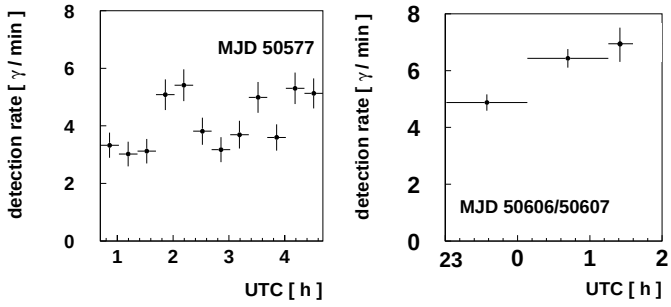


**Fig. 19.** The $\gamma$-ray detection rate of the two nights: MJD = 50576/50577 (May 8th/9th) and 50606/50607 (June 7th/8th). For the first night, a 20 minutes binning and for the second night, a 67 minutes binning has been used.

## 6. Correlation of the TeV emission with the X-ray emission

A correlation of X-ray and TeV fluxes would give clues regarding the emission mechanism. The All Sky Monitor on board the *Rossi X-Ray Timing Explorer* has been regularly observing bright X-ray sources in the energy range from 2 - 12 keV since January 5th, 1996. It observed mainly X-ray binaries and a list of initially 10, and since May 1997 a list of 74 bright active galactic nuclei. Each object is monitored roughly 5 times a day, each time for 90 seconds. The detection threshold per 90 second observation is 30 mCrab. The ASM data is publicly available over the Internet.

The ASM monitors Mkn 501 since January 5th, 1996. In Fig. 20 the time histories of the ASM flux and the hardness ratio *counts*(5-12.1 keV) / *counts*(1.3-3.0 keV), both computed with bins of 1 week duration, are compared to the light curve of the HEGRA IACT-system. We derived the ASM count rates $r_{\rm X}$ from the "definitive" ASM products satisfying the requirement of a dwell duration larger than 30 s and a flux fit with a reduced $\chi^2$-value smaller than 1.25. We excluded days with poor sampling (less than 25% of the data), by using only the diurnal rates values which have an error smaller than 0.375 counts/sec. The binned light curves, hardness ratios, and correlation coefficients ("slow" method with error propagation) have been obtained using the "ftools 4.0" package.

The count rate increases from 0.4/sec in February, 1996, slowly to 1 counts/sec in January, 1997, and then dramatically to 2 counts/sec in June/July 1997. After reaching its maximum of 3.1±0.4 on June 24th, 1997, the count rates returned to around 1 counts/sec until April 1998. During the major flaring phase in 1997, the X-ray spectrum hardens, i.e. the hardness ratio increases from 0.8 in January 1997 to 1.5 in July 1997 and decreases again to 1 until April 1998.

A correlation between the X-ray activity and the TeV-activity can be recognized in the sense that the X-ray activity peaked in June/July when the amplitudes of the TeV flares reached their maximum.

In Fig. 21 the correlation between the daily differential flux at 2 TeV, $\Phi_{2\,\rm TeV}$, and the count rate $r_{\rm X}$ is shown. Hereby, for each daily $\Phi_{2\,\rm TeV}$-value, the ASM rate has been averaged over all 90 second measurements within the 24 h time interval centered close to 0:00 UT. One sees indications of a correlation between the emission in the two energy bands. A fit to the data gives the correlation:

$$r_{\rm X}\,[\rm counts/sec] = 0.94^{+0.05}_{-0.06} + (2.7 \pm 0.3) \times \frac{\Phi_{2\,\rm TeV}}{10^{-10}\,\rm cm^{-2}\ s^{-1}\ TeV^{-1}}. \quad (8)$$

A possible time shift $\Delta t$ between the TeV- and X-ray variability has been searched for by computing the discrete correlation function, DCF, (Edelson & Krolik 1988)

$$\xi\,(\Delta t) = \frac{\sum_i (\Phi_{2\,\rm TeV}(t_i) - \overline{\Phi_{2\,\rm TeV}})(r_{\rm X}(t_i+\Delta t) - \overline{r_{\rm X}})}{\sqrt{\sum_i (\Phi_{2\,\rm TeV}(t_i) - \overline{\Phi_{2\,\rm TeV}})^2 \ \sum_i \ (r_{\rm X}(t_i+\Delta t) - \overline{r_{\rm X}})^2}} \quad (9)$$

as function of $\Delta t$. The index $i$ runs over all nights with TeV-measurements, the $\Phi_{2\,\rm TeV}(t_i)$ are the daily TeV flux amplitudes, and the $r_{\rm X}(t_i)$ are the ASM count rates averaged over 24 h, centered close to 0:00 UT. In Fig. 22 the results are presented. The DCF shows a positive peak reaching from $\Delta t = -1$ (TeV variability follows X-ray variability after 1 day) to $\Delta t = 1$ (TeV variability precedes X-ray variability by one day).

The data indicates a correlation of the TeV- and X-Ray emission with a time lag of one day or less. For $\Delta t = 0$, 50 pairs of TeV and X-ray data enter the calculation and give a DCF of 0.37±0.03. Even completely uncorrelated time series are expected to produce non-zero values of the DCF (Edelson & Krolik 1988). The probability distribution of the DCF depends on the number of pairs used for its calculation and on the temporal autocorrelation characteristics of the TeV emission and the X-ray emission. Assuming 50 statistically independent flux measurements in two energy bands which follow Gaussian distributions around their mean values, the chance probability for DCF-values exceeding 0.37±0.03 is 0.43%. Reducing the number of statistically independent flux pairs from 50 to 15, increases this chance probability to 8%. The true chance probability of the correlation indicated in Figs. 21 and 22 will lie between these two

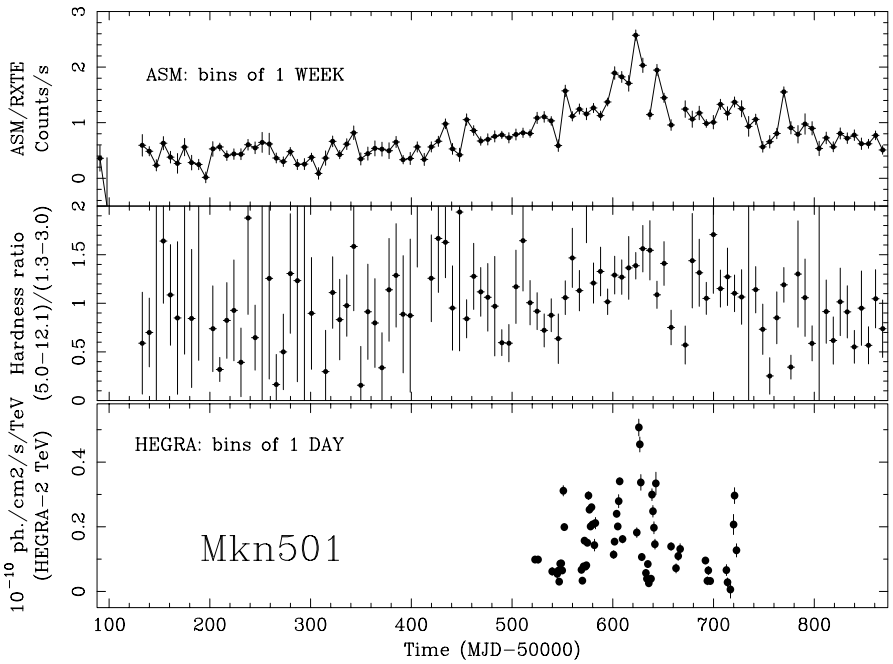


**Fig. 20.** The ASM count rates $r_{\rm X}$ (2-12 keV), the ASM hardness ratios *counts*(5-12.1 keV) / *counts*(1.3-3.0 keV), and the daily HEGRA differential fluxes at 2 TeV against time, for the time period from January 1997 until February 1998.

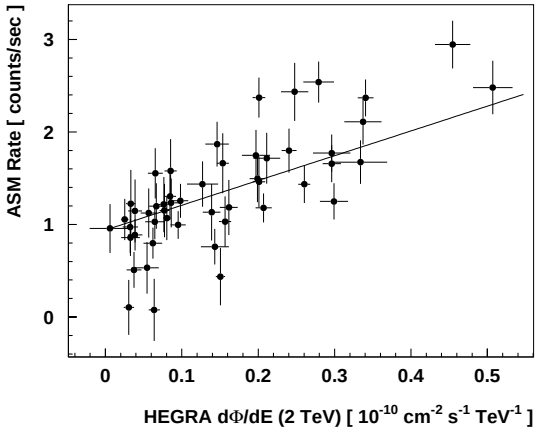


**Fig. 21.** The correlation of the one-day ASM count rates $r_{\rm X}$ (2-12 keV) with the daily HEGRA differential fluxes at 2 TeV. Superimposed is a straight line fit to the data.

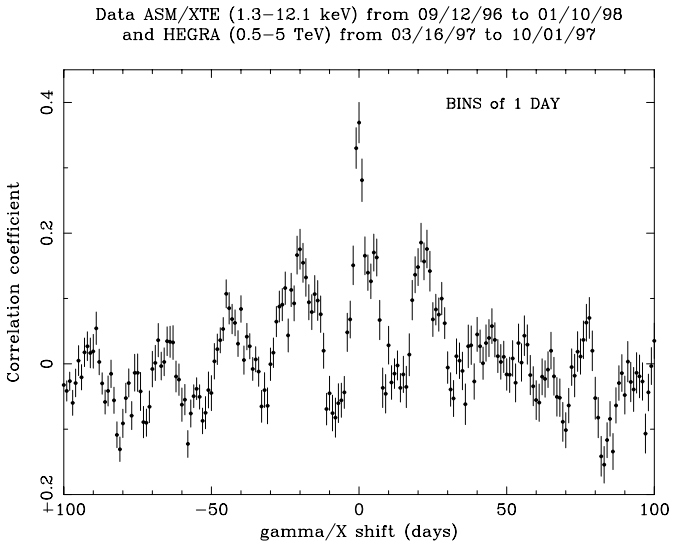


**Fig. 22.** The correlation coefficient of the daily HEGRA differential fluxes at 2 TeV and the one-day ASM count rates $r_{\rm X}$ (2-12 keV) as a function of the time shift $\Delta t$ between the considered TeV and X-ray fluxes. Positive $\Delta t$-values correspond to the TeV variability preceding the X-ray variability.

extremes. Note, that the same correlation is found in the CT1 data and in the CT2 data (see Part II).

We interpret the structure of the DCF which can be recognized in Fig. 22 as to arise from the periodic gaps in the HEGRA observation time, paired with the spiky structure of the Mkn 501 light curve in both energy bands.

## 7. Discussion

The observations of Mkn 501 during its remarkable state of flaring activity in 1997 with the HEGRA IACT system allowed us to study in detail the temporal and spectral characteristics of the source with, for gamma-ray astronomy, unprecedented photon statistics and precision. More than 38,000 TeV $\gamma$-ray photons were detected during March 1997 until October 1997. These photons enabled the localization of the $\gamma$-ray source with an accuracy of about 40 arc seconds.

The mean flux of $\gamma$-rays averaged over the whole period of activity was as high as three times the flux of the Crab Nebula, the strongest persistent TeV source in the sky. For a source of this strength, even "loose" shape cuts result in an almost background free detection of $\gamma$-rays: several 100 $\gamma$-rays against 20 background events caused by cosmic rays. This implies the statistically significant detection of the source every few minutes during the whole 6 months of observations and makes it

possible to study the flux variability on sub-hour time scales. Furthermore, the good precision of reconstruction of the energy of *individual* $\gamma$-rays with $20\%$ resolution combined with high $\gamma$-ray statistics makes it possible to measure the energy spectra of the radiation and their evolution in time on a night-by-night basis.

In this paper we presented the results obtained from IACT system data. The data of CT1 and CT2 are described in Part II. The IACT system data has not given any evidence for a correlation between the emission intensity at 2 TeV and the spectral index, determined between 1 and 5 TeV. The study of the time gradient of the diurnal flux at 2 TeV yielded shortest increase/decay times of the order of 15 h. A dedicated search for short time variability within individual nights yielded evidence for a variability with a corresponding increase/decay time of the order of 5 h. The data indicated a weak correlation between the TeV-flux amplitudes and the 2 to 12 keV X-ray flux, fovouring a time lag between the TeV- and the X-ray variability of one day or less. In the following we will briefly discuss these results.

### *7.1. Spectral characteristics*

Commonly it is believed that the study of the TeV $\gamma$-ray spectra of BL Lac objects at different epochs of their activity provides key insights into the nature of the $\gamma$-ray production processes in the relativistic jets. Generally, in these highly dynamical objects, when the flux could be changed by an order of magnitude within 1 day of observations, strong time-variation of the spectral shape of the radiation is expected as well. However, the average spectra of Mkn 501 in the energy range from 1 TeV to 10 TeV corresponding to largely different absolute flux levels, appear to be very similar as discussed in Sect. 4 (see Fig. 13).

In the framework of Inverse Compton models this could be interpreted as result of (1) a time-independent spectrum of accelerated electrons, together with (2) a very fast radiative cooling of the electrons which establishes an equilibrium spectrum of electrons during the time required for the collection of sufficient photon statistics for proper spectral measurements (typically a few hours or less if the absolute $\gamma$-ray flux exceeds the flux level of the Crab). At first glance, this contradicts the observed dramatic shift of the synchrotron peak in the Mkn 501 spectrum by 2 orders of magnitude in frequency, discovered with BeppoSAX during the April 1997 flaring phase (Pian et al. 1998). Formally speaking, the position of the synchrotron peak $\nu_{\rm s}$ is proportional to $B\,\delta_{\rm j}\,E^2_{\rm max}$, henceforth its variation could be explained by the variation of any of the three appropriate parameters - magnetic field $B$, Doppler factor $\delta_{\rm j}$, and the maximum energy of accelerated electrons $E_{\rm max}$. However as it was argued by Pian et al. (1998), the shift of the synchrotron peak during these specific observations could hardly be attributed to the variation of the Doppler factor and/or magnetic field, but is caused rather by an increase (by a factor of 10 or so) of the maximum energy of accelerated electrons. On these grounds we may expect a significant hardening of the TeV spectrum as well. However, due to the Klein-Nishina cross-section, the increase of $E_{\rm max}$ in the IC spectrum is expected to be substantially less pronounced.

It should be emphasized, that during the whole period of 1997 the source was in a "high" state with a TeV flux $\geq 1\,{\rm Crab}$. It will be of utmost interest to use the IACT system to study the Mkn 501 spectrum in a really low state, characterized by a TeV flux well below one Crab unit.

The second interesting feature of the *flux-selected* spectra averaged over almost 6 months of observations (Fig. 13) is their smooth shape with power-law photon index of about $\alpha = -2.25$ ($\mathrm{d}N_\gamma\,/\,\mathrm{d}E \propto E^\alpha$) at energies between 1 TeV and several TeV, *but* with a gradual steepening at higher energies. We would like to make a comment concerning the implications of the steepening of the spectrum for the estimates of the diffuse extragalactic background radiation (DEBRA). If one interprets the lack of a cutoff in the $\gamma$-ray spectra of both Mrk 421 (Zweerink et al. 1997) and Mrk 501 (Aharonian et al. 1997a) up to 10 TeV as an indication for the absence of absorption in the DEBRA, an upper limit on the energy density of DEBRA, $u_\epsilon = \epsilon^2 n(\epsilon) \simeq 10^{-3}\,{\rm eV/cm^3}$ at $\lambda \sim 10\,\mu{\rm m}$ can be derived from the condition of the transparency of the intergalactic medium for 10 TeV $\gamma$-rays (Weekes et al. 1997). The recent studies of the problem, based on different assumptions about the spectral shape of the DEBRA, give similar results (Stanev &Franceschini 1997; Funk et al. 1998; Biller et al. 1998; Stecker & De Jager 1998). However, as it was emphasized by Weekes et al. (1997), the lack of an apparent cutoff in $\gamma$-ray spectra does not automatically imply negligible intergalactic absorption. Indeed, some infrared background models, like the *cold+hot dark matter* model of Macminn & Primack (1996), predict a *modulation* rather than *cutoff* in the spectra of Mrk 421 and Mrk 501. The absorption results in a steepening of the $\gamma$-ray spectrum, but a power-law form could be conserved, at least up to 10 TeV. Also, the revised estimate of the effect of the intergalactic absorption by Stecker and De Jager (1998) based on an empirically derived flux of the DEBRA (Malkan & Stecker 1998), does not produce a cutoff until $\simeq$15 TeV.

The general tendency of gradual steepening of the spectra of Mrk 501 obtained in this paper could be formally interpreted as a result of absorption in the intergalactic background radiation, which would allow to estimate the density of the DEBRA. Obviously this number could not be far from the above upper limit estimate. However, care should be taken in the interpretation of these results, since the intrinsic spectra of the source are not properly understood and probably several effects combine to steepen the TeV spectra of BL Lac objects.

### *7.2. Temporal characteristics*

Our observations revealed flux variability on time scales $\Delta t_{\rm obs}$ of between 5 and 15 h. Due to causality and light travel time arguments the size of the $\gamma$-ray production region cannot exceed

$$R = \Delta t_{\rm obs} c\,\delta_{\rm j} \simeq 3\cdot 10^{15}\,\Delta t_{10}\,\delta_{\rm j}\,{\rm cm}, \qquad (10)$$

with $\Delta t_{10} = \Delta t_{\rm obs}/10\,{\rm h}$ and where $\delta_{\rm j}$ is the Doppler factor of the jet. The condition that the source is optically thin with respect to photon-photon pair production, $\tau_{\gamma\gamma} \leq 1$, results in a *lower limit* on the Doppler factor of the jet $\delta_{\rm j}$, assum-

ing that the low-frequency photons are produced co-spatially in the quasi-isotropically emitting cloud (blob): $\delta_{\rm j,min} \simeq 6 F_{-10}(\epsilon)^{1/6}\,\Delta t_{10}^{-1/6}$ (see e.g. Celotti et al. 1998), where $F_{-10}(\epsilon) = F_{\rm obs}(\epsilon)/\ 10^{-10}\,{\rm erg/cm^2 s}$ is the observed energy flux of the optical and the infrared photons at the observed energy $\epsilon = 2 m_{\rm e}^2\,c^4\,\delta_{\rm j,min}^2/E_\gamma \simeq 5\,(\delta_{\rm j}/10)^2\,(E_\gamma/10\,{\rm TeV})^{-1}\,{\rm eV}$ with width $\Delta\epsilon \simeq \epsilon$; $E_\gamma$ is the energy of detected $\gamma$-ray photon. The characteristic fluxes of the optical and the infrared radiation from Mkn 501 of about $0.5 \cdot 10^{-10}\,{\rm erg/cm^2 s}$ (see e.g. Pian et al. 1998), and the time variability of the 1-10 TeV $\gamma$-rays within 5 to 15 h obtained above, require a minimum Doppler factor in the order of 5. Due to the weak dependence of $\delta_{\rm j,min}$ on $F_{\rm obs}$ and $\Delta t_{\rm obs}$, we can not expect a further significant strengthening of this lower limit on $\delta_{\rm j}$.

On the other hand, if the TeV $\gamma$-rays are produced by relativistic electrons which up-scatter their low-frequency synchrotron radiation (the so-called Synchrotron Self Compton (SSC) scenario, see e.g. Ghisellini et al. 1996; Bloom & Marscher 1996; Inoue & Takahara 1996; Mastichiadis & Kirk 1997; Bednarek & Protheroe 1997), the observed time variability of TeV $\gamma$-rays sets also a strong *upper limit* on the Doppler factor, if one requires that the synchrotron and Compton cooling time of the electrons is smaller than the flux variability time. Indeed, the energy density of the low-frequency target photons in this model is estimated as $w_{\rm r} \simeq (d/R)^2 F_{\rm obs} c^{-1} \delta_{\rm j}^{-4}$, where $d$ is the distance to the source ($\simeq 170\,{\rm Mpc}$ for $H_0 = 60\,{\rm km/s\,Mpc}$), $R$ is the size of the $\gamma$-ray production region which is limited by Eq. 10, but most probably cannot be significantly less than $R_{15} = R/10^{15}\,{\rm cm}$. Assuming that the synchrotron and Compton cooling time of electrons $t = [(4/3)\sigma_{\rm T}(w_{\rm r} + B^2/8\pi)E_{\rm e}/m_{\rm e}^2 c^4]^{-1} \simeq 15\,((w_{\rm r} + B^2/8\pi)/1\,{\rm erg/cm^3})^{-1}\,(E_{\rm e}/1\,{\rm TeV})^{-1}$ s, where $B$ is the magnetic field in the jet, does not exceed the flux variability time (in the frame of the jet) $\Delta t' = \Delta t_{\rm obs}\,\delta_{\rm j}$, we find

$$\delta_{\rm j,max} \simeq 75\,F_{10}^{1/3}\,R_{\rm min,15}^{-2/3}\,\Delta t_{10}^{1/3}\left(\frac{E_{\rm e}}{1\,{\rm TeV}}\right)^{1/3}\left(\frac{F_{\rm X}}{F_{\rm TeV}}\right)^{1/3} \quad (11)$$

where $F_{\rm X}/F_{\rm TeV}$ is the ratio of the energy flux emitted in the X-ray band and in the TeV band. For characteristic values of $F_{10} \simeq 0.5$, $R_{\rm min,15} \simeq 3$, $\Delta t_{10} \simeq 1$, $E_{\rm e} \simeq 1$ TeV, and $F_{\rm X}/F_{\rm TeV} \simeq 5$ (Pian et al. 1998) one obtains $\delta_{\rm j,max} \simeq 50$.

In their different modifications, the inverse Compton (IC) models of TeV radiation of BL Lac objects predict the correlation between the X-ray- and TeV-regimes which is indicated in Figs. 21 and 22. Albeit a correlation X/TeV is a strong argument in favor of the common *electronic* origin of the parent particles which produce synchrotron X-rays and IC $\gamma$-rays, the fact of the correlation alone does not decide definitively between the electronic and hadronic nature of the primary (accelerated) particles. For example in *Proton Blazar* type models (Mannheim 1993), the bulk of the nonthermal emission is produced at later stages of the proton-induced-cascade through the same synchrotron and IC radiation of the secondary (cascade) electrons.

In fact, the short time variability of the keV/TeV-radiation strongly argues in favor of electronic models. Whereas the fast radiative (synchrotron and IC) cooling time of the electrons in the jet readily match the observed time-variability on a time scale of some hours, the inelastic hadron interactions, both with ambient gas or photon fields are rather slow processes and only become effective at very high target gas densities and/or photon densities, exceeding significantly the typical values characterizing the $\gamma$-ray emitting jets in BL Lac objects (Schlickeiser 1996; Sikora 1997). Nevertheless, presently the hadronic models cannot be ruled out unambiguously on the basis of arguments concerning the time variability of the TeV-flux. The rapid variability can be explained by geometrical effects, e.g., by anisotropies in the comoving frame of the jet (Salvati et al. 1998), or in models where the flares occur due to fast moving targets (gas clouds) which cross the beam of relativistic particles (Dar & Laor 1997).

*Acknowledgements.* We thank the Instituto de Astrofísica de Canarias (IAC) for supplying excellent working conditions at La Palma. We gratefully acknowledge the work of the technical support staff of Heidelberg, Kiel, Munich and Yerevan. HEGRA is supported by the BMBF (Germany) and CYCIT (Spain). The correlation analysis of the TeV flux and the RXTE ASM X-ray flux has used data obtained through the High Energy Astrophysics Science Archive Research Center Online Service, provided by the NASA/Goddard Space Flight Center.

## References

Aharonian F.A., Akhperjanian A.G., Barrio J.A., et al., 1997a, A&A 327, L5
Aharonian F.A., Hofmann W., Konopelko A.K., Völk H.J., 1997b, Astropart. Phys. 6, 343
Aharonian F.A., Akhperjanian A.G., Barrio J.A., et al., 1997c. In: Proc. 4th Compton Symposium, AIP Conf. Proc., Dermer C., Strickman M., Kurfess J. (eds), 1397
Aharonian F.A., Akhperjanian A.G., Barrio J.A., et al., 1998, submitted to Astropart. Phys.
Barrau A., Bazer-Bachi R., Cabot H., et al., 1997, astro-ph/9710259
Bednarek W., Protheroe R.J., 1997, MNRAS 287, L9
Bhat C.L., Koul R., Kaul R.K., et al., 1997. In: Procs. Towards a Major Atmospheric Cherenkov Detector V, De Jager O.C. (ed), Kruger Park, South Africa
Biller S.D., Buckley J., Burdett A., et al., 1998, Phys. Rev. Lett. 80, 2992
Bloom S.D., Marscher A.P., 1996, ApJ 461, 657
Bradbury S.M., Deckers T., Petry D., et al., 1997, A&A 320, L5
Buckley J.H., Akerlof C.W., Biller S., et al., 1996, ApJ 472, L9
Bulian N., Daum A., Hermann G., et al., 1998, Astropart. Phys. 8, 223
Catanese M., Bradbury S.M., Breslin A.C., et al., 1997, ApJ 487, L143
Catanese M., Akerlof C.W., Badran H.M., et al., 1998, ApJ 501, 616
Celotti A., Fabian A.C., Rees M.J., 1998, MNRAS 93, 239
Collura A., Rosner R., 1987, ApJ 315, 340
Dar A., Laor A., 1997, ApJ 478, L5
Daum A., Hermann G., Heß M., et al., 1997, Astropart. Phys. 8, 1
Edelson R.A., Krolik J.H., 1988, ApJ 333, 646
Fegan D.J., 1996, Space Sci. Rev. 75, 137
Fraß A., Köhler C., Hermann G., Heß M., Hofmann W., 1997, Astropart. Phys. 8, 91
Funk B., Magnussen N., Meyer H., et al., 1998, Astropart. Phys. 9, 97
Gaidos J.A., Akerlof C.W., Biller S., et al., 1996, Nat 383, 319
Ghisellini G., Maraschi L., Dondi L., 1996, A&AS 120, 503
Hayashida N., Hirasawa H., Ishikawa F., et al., 1998, astro-ph/9804043
Hemberger M., 1998, PhD thesis, Universität Heidelberg, Germany

Hillas A.M., 1985. In: Proc. 19th ICRC, La Jolla 3, 445
Inoue S., Takahara F., 1996, ApJ 463, 555
Konopelko A., 1995. In: Proc. Towards a Major Atmospheric Cherenkov Detector-IV, Cresti M. (ed), 373
Konopelko A., Aharonian F.A., Akhperjanian A., et al., 1996, Astropart. Phys. 4, 199
Konopelko A., Hemberger M., Aharonian F.A., et al., 1998, submitted to Astropart. Phys.
Macminn D., Primack J.R., 1996, Space Sci. Rev. 75, 413
Malkan M.A., Stecker F.W., 1998, ApJ 496, 13
Mannheim K., 1993, A&A 269, 67
Mastichiadis A., Kirk J.G., 1997, A&A 320, 19
Mirzoyan R., Kankanian R., Krennrich F., et al., 1994, NIM A 315, 513
Pian E., Vacanti G., Tagliaferri G., et al., 1998, ApJ 492, L17
Petry D., Bradbury S.M., Konopelko A., et al., 1996, A&A 311, L13
Pühlhofer G., Daum A., Hermann G., et al., 1997, Astropart. Phys. 8, 101
Punch M., Akerlof C.W., Cawley M.F., et al., 1992, Nat 358, 477
Protheroe R.J., Bhat C.L., Fleury P., et al., 1997, 25th ICRC, Durban 1997, astro-ph/9710118
Quinn J., Akerlof C.W., Biller S., et al., 1996, ApJ 456, L83
Rauterberg G., Müller N., Deckers T., et al., 1995. In: Proc. 24th ICRC, Rome, 3, 460
Remillard R.A., Levine M.L., 1997, astro-ph/9707338
Samuelson F.W., Biller S.D., Bond I.H., 1998, ApJ 501, L17
Salvati M., Spada M., Pacini F., 1998, ApJ 495, L19
Schlickeiser R., 1996, Space Sci. Rev. 75, 299
Sikora M., 1997. In: Proc. 4th Compton Symposium, AIP Conf. Proc., Dermer C., Strickman M., and Kurfess J. (eds), 494
Stanev T., Franceschini A., 1998, ApJ 494, L159
Stecker F.W., De Jager O.C., 1998, A&A 334, L85
Takahashi T., Tashiro M., Madejski G., et al., 1996, ApJ 470, L89
Ulrich M.H., Maraschi L., Urry C.M., 1997, ARA&A 35, 445
Urry C.M., Padovani P., 1995, PASP 107, 803
Weekes T.C., Aharonian F.A., Feegan D.J., Kifune T., 1997. In: Proc. 4th Compton Symposium, AIP Conf. Proc., Dermer C., Strickman M., Kurfess J. (eds), 361
Wiebel-Sooth B., Biermann P.L., Meyer H., 1998, A&A 330, 389
Zweerink J.A., Akerlof C.W., Biller S.D., et al., 1997, ApJ 490, L144